https://doi.org/10.5194/egusphere-2026-975
Preprint. Discussion started: 27 March 2026

Water storage trends derived from the GRACE/-FO global gravity-based groundwater product (G3P)

Roland Hohensinn[a,e,*], Junyang Gou[b,c], Ulrich Meyer[d], Vincent Humphrey[f], Wouter Dorigo[g], Eva Boergens[e], Benedikt Soja[b], Alexander Gruber[g], Laura Jensen[e], Annette Eicker[e,i], Michael Rast[a], Andreas Güntner[e,h]

[a]*International Space Science Institute, Hallerstrasse 6, Bern, 3012, Switzerland*
[b]*Institute of Geodesy and Photogrammetry, ETH Zurich, Robert-Gnehm-Weg 15, Zurich, 8093, Switzerland*
[c]*Department of Earth, Atmospheric and Planetary Sciences, Massachusetts Institute of Technology, 77 Massachusetts Avenue, Cambridge, 02139, USA*
[d]*Astronomical Institute, University of Bern, Sidlerstrasse 5, Bern, 3012, Switzerland*
[e]*GFZ Helmholtz Centre for Geosciences, Telegrafenberg, Potsdam, 14473, Germany*
[f]*Federal Office of Meteorology and Climatology MeteoSwiss , Operation Center 1, Zürich-Flughafen, 8058, Switzerland*
[g]*Department of Geodesy and Geoinformation, TU Wien , Wiedner Hauptstrasse 8-10, Wien, 1040, Austria*
[h]*University of Potsdam, Institute of Environmental Science and Geography , Karl-Liebknecht-Strasse 24-25, Potsdam, 14476, Germany*
[i]*HafenCity University Henning-Vorscherau-Platz 1, Hamburg, 20457, Germany*

Abstract

The Global Gravity-based Groundwater Product (G3P) provides observations of global groundwater storage (GWS) variations, calculated from GRACE/-FO-derived terrestrial water storage (TWS) by subtracting the contributions of root zone soil moisture, glaciers, surface water storage, and snow water equivalent. As such, G3P provides the first globally consistent, publicly available groundwater dataset from satellite gravimetry for continental-scale trend assessment. Such data are a crucial observational constraint for assessing global groundwater depletion, recharge, and water storage trends related to climate change and human activities.

A challenge is the reliable separation and quantification of long-term trends from stochastic signals attributable to natural climate variability ("climate noise") and observational system errors. To address this, we introduce a trend-analysis framework that uses calibrated time-series models to account for trends, seasonal, and stochastic variations. The approach requires minimal assumptions about underlying processes and enables the separation of significant long-term trends of GWS and TWS from stochastic variability.

Applying this framework to 21.5 years of data, our results show (1) that groundwater depletion dominates freshwater decline at continental scales – most prominently in Asia (-55 km^3 yr^{-1}) – whereas ice mass loss remains the largest global contributor by component, and (2) reveal previously unobserved trends, including increasing groundwater storage in large parts of Africa ($+37$ km^3 yr^{-1}) and declining trends attributed to droughts, e.g., in Southern Africa, Asia, and parts of Europe. Our global aggregation of statistically significant trends indicates net volumetric GWS changes of -27 km^3 yr^{-1} and TWS changes of -145 km^3 yr^{-1} (excluding Antarctica and Greenland). We also find that many regions in the Northern Hemisphere are prone to climate-induced drying, with parts of Europe close to persistent long-term groundwater decline.

Keywords: GRACE/-FO hydrology, terrestrial water storage (TWS), groundwater storage (GWS), freshwater resources, climate change, hydrological signal decomposition, trend analysis

*Correspondence to: Roland Hohensinn (roland.hohensinn@gfz.de)

https://doi.org/10.5194/egusphere-2026-975
Preprint. Discussion started: 27 March 2026

1. Introduction

1.1. Water storage as an Essential Climate Variable and its observation with satellite gravimetry

Quantifying trends in terrestrial water storage (TWS) is central for assessing changes in global freshwater availability and its coupling to the climate system (Rodell et al., 2018; Pokhrel et al., 2021; Huggins et al., 2022; Riva et al., 2010; Frederikse et al., 2020; Gou et al., 2025; Seo et al., 2025; Humphrey et al., 2023). TWS integrates changes in groundwater storage (GWS), soil moisture, surface water, snow water equivalent, and glaciers (Tapley et al., 2019). To reflect their importance, TWS and GWS have been endorsed as Essential Climate Variables by the Global Climate Observing System (GCOS) (Zemp et al., 2022).

Since 2002, the GRACE (2002–2017) and GRACE Follow-On (since 2018) missions provide global observations of time-variable mass change (Tapley et al., 2004; Landerer et al., 2020), yielding an almost continuous over-two-decade record that substantially improves trend detectability compared to earlier GRACE-only studies. Within the Global Gravity-based Groundwater Product (G3P), consistent global GWS estimates (v1.11–v1.12) are derived from GRACE/-FO TWS by subtracting filtered contributions of other storage compartments (Güntner et al., 2026). GRACE/-FO observations capture the combined effects of climate-driven ice and glacier mass loss, anthropogenic water use (e.g., groundwater extraction for irrigation), and natural variability in precipitation and recharge (e.g., Rodell et al. 2018; Li and Rodell 2024). For global trend assessment, GRACE/-FO observations are particularly valuable because hydrological and land-surface models can exhibit divergent trend signs and magnitudes (e.g., soil moisture; Albergel et al. 2012), which complicates trend inference (Scanlon et al., 2018).

1.2. Observed global and continental-scale patterns in TWS and GWS

GRACE-based assessments reveal spatially heterogeneous TWS trends. For 2002–2016, global land water storage losses of approximately -154 ± 22 km^3/yr can be deduced from Rodell et al. 2018 (excluding Antarctica and Greenland), largely driven by ice mass loss in North America. Continental patterns include strong negative trends in Asia (exceeding -50 km^3/yr) and comparable magnitudes in North America, where cryospheric processes dominate (Rodell et al., 2018). In contrast, Africa shows positive anomalies in parts of the Sahel and East Africa, attributed to precipitation variability and enhanced groundwater recharge – the so-called Sahelian Paradox (Werth et al., 2017; Springer et al., 2023; Boergens et al., 2024a). South America exhibits moderate losses dominated by Patagonian glacier retreat, while strong variability driven by El Niño Southern Oscillation (ENSO) is a complicating factor for detection in the Amazon Basin (Tapley et al., 2019; Satizábal-Alarcón et al., 2024). Regarding recent synthesis efforts, Chandanpurkar et al. 2025 reported a continental TWS loss (excluding Greenland and Antarctica) exceeding 300 km^3 yr^{-1}, representing one of the largest published global land TWS loss estimates to date.

GWS represents a critical and regionally heterogeneous component of TWS change. Global anthropogenic groundwater depletion has been estimated at approximately 100–150 km^3/yr during the early 21st century, with some model-based estimates reaching up to about 200 km^3/yr (Döll et al., 2014; de Graaf et al., 2017; Bierkens and Wada, 2019). However, regional groundwater gains partly offset these losses, resulting in substantially smaller net global groundwater storage declines. While groundwater represents roughly 15–25% of total global land water mass losses when ice-sheet contributions are included, it dominates TWS decline across non-glaciated continental regions at a contribution of about 65% (Chandanpurkar et al., 2025). Large-scale syntheses based on groundwater well observations confirm widespread groundwater decline, along with localized recovery resulting from policy interventions (Jasechko et al.,

https://doi.org/10.5194/egusphere-2026-975
Preprint. Discussion started: 27 March 2026

2024). Major depletion hotspots are the Indo-Gangetic Plain, North China Plain, and the Middle East (Rodell et al., 2009; Feng et al., 2013a; Joodaki et al., 2014; Gou and Soja, 2024), as well as the High Plains Aquifer and California's Central Valley in North America (Scanlon et al., 2012; Famiglietti et al., 2011). In Africa, positive GWS anomalies in parts of the Niger Basin and the East African Rift are in contrast to depletion in North African fossil aquifer systems, notably the North Western Sahara Aquifer System (NWSAS) and the Nubian Sandstone Aquifer System (NSAS)(Werth et al., 2017; Springer et al., 2023).

1.3. Physical drivers, attribution, and limits of interpretability

Attribution of TWS and GWS trends to climate-related versus anthropogenic drivers is important, but a challenging task. Cryospheric mass loss is the dominant component of global TWS decline, with Greenland (∼–279±23 km^3/yr) and Antarctica (∼–128±40 km^3/yr), together with mountain glaciers, which drives an accelerated mass loss under climate warming (Rodell et al., 2018; Chen et al., 2006; Otosaka et al., 2022). Outside glaciated regions, irrigation-driven groundwater extraction is the dominant contributor to negative trends, and is reported to exceed natural recharge by factors of 2–10 (Wada et al., 2012; Richey et al., 2015).

Climate variability linked to large-scale modes such as ENSO, the North Atlantic Oscillation (NAO), and the Indian Ocean Dipole (IOD) is known to modulate precipitation, soil moisture, surface water, and groundwater recharge on interannual to decadal time scales (Anyah et al., 2018; Boergens et al., 2024b). Assessments indicate that, when integrating across storage compartments, climate forcing may exceed anthropogenic contributions to decadal land water storage change, although this is reported to strongly depend on the region (Scanlon et al., 2018). TWS trends also propagate into sea-level budgets and Earth-system mass closure, providing constraints on coupled hydrosphere–cryosphere processes (Riva et al., 2010; Frederikse et al., 2020; Gou et al., 2025; Seo et al., 2025), however uncertainties across storage components remain substantial (Dorigo et al., 2021).

Hydrological memory is a limiting factor for trend interpretation: groundwater and glaciers integrate multi-year climate signals, whereas soil moisture and surface water respond more rapidly. These memory effects – often underrepresented in models – can generate long-period-transient-type apparent-secular trends in records of limited duration (Lu et al., 2025; Humphrey and Gudmundsson, 2019; Vishwakarma et al., 2021). This a strong motivation for the use of statistical frameworks that explicitly account for persistence and stochastic variability (Franzke, 2012; Humphrey et al., 2017).

1.4. Detectability limits and the role of natural variability and observational errors

GRACE/-FO trend magnitudes are typically small relative to seasonal and interannual variability, motivating additive decompositions into trends, periodic signals, and residual variability from climate and observational noise (Steffen et al., 2009; Humphrey et al., 2016; Scanlon et al., 2016). Representative global studies combining such decompositions with trend-significance testing show that, although basin-scale trends are often within ±20 mm/yr compared to seasonal amplitudes of up to ∼250 mm, statistically significant trends are nevertheless widespread (Scanlon et al., 2016). The trend-to-variability ratio (TVR) further highlights that trend magnitude alone can misidentify water-stress hotspots when natural variability is large (Vishwakarma et al., 2021).

Persistent stochastic variability and long-range memory can inflate trend uncertainties and produce apparent trends over finite records (Mandelbrot and Wallis, 1969; Franzke, 2012; Mudelsee, 2010; Humphrey et al., 2017). Long-memory behavior ("Hurst effect") motivates the use of parametric noise models such as ARFIMA or simpler AR(1) processes (Koutsoyiannis, 2003; Franzke and O'Kane, 2017; Orth et al., 2013). Colored noise has been identified in

https://doi.org/10.5194/egusphere-2026-975
Preprint. Discussion started: 27 March 2026

GRACE-derived TWS time series, resulting in underestimated uncertainties if autocorrelation is ignored (Gunes and Aydin, 2024). Generalized least squares (GLS) approaches that explicitly model the covariance structure are therefore very well suited under the presence of stochastic memory (Mudelsee, 2019), while least-squares regression remains robust even under moderate departures from normal distribution properties (Knief and Forstmeier, 2021).

1.5. Research gap and study objectives

Accurate and reliable global trend inference and water storage change quantification from GRACE/-FO remains challenging by the presence of persistence and long-range memory, which can yield underestimated uncertainties and false-positive detections when not modeled explicitly (Mandelbrot and Wallis, 1969; Franzke, 2012; Humphrey et al., 2017; Mudelsee, 2010). These limitations are critical for detection and attribution (D&A) studies aiming to separate externally forced change from internal variability (Bindoff et al., 2014). While optimal fingerprinting is well established for temperature and precipitation (Hasselmann, 1997; Allen and Tett, 1999), its application to TWS and GWS is hindered by uncertainties in modeled storage variability (Humphrey et al., 2017; Scanlon et al., 2018; Jensen et al., 2019).

Here, we introduce a statistically traceable trend-detection framework for GRACE/-FO-derived water storage time series that explicitly accounts for short- and long-range memory using GLS with autocovariance modeling. Leveraging the G3P data, we provide a consistent, uncertainty-aware assessment, quantification and attribution of groundwater storage trends by jointly analysing GWS and TWS, as well as its contributing storage compartments – root-zone soil moisture, glacier mass, snow water equivalent, and surface water storage (Güntner et al., 2024). While for earlier GRACE studies trend interference and change quantification has often been limited due to the limited dataset lengths, we now can access 20+ years of GRACE/-FO time series data, and a globally available GRACE-derived GWS dataset. By applying the same framework to TWS and other storage time series, we demonstrate scalability to other essential climate variables (Bindoff et al., 2014).

Section 2 describes the G3P data products and the mathematic-statistical detection framework. Section 3 analyses spatio-temporal and spectral characteristics of TWS and GWS data, and presents global and regional significant trends, attributes drivers, and quantifies volumetric changes. Section 4 summarizes the added value of this study and outlines future research. Supplementary sections, figures, tables, and equations are indicated by the prefix "S".

2. Data and Methods

2.1. G3P Data

For obtaining gridded, spherical-harmonics-based time series of TWS and GWS variations, the GFZ and G3P data processing workflow for the GRACE and GRACE-FO missions follows a hierarchical approach. First, raw satellite observations are transformed into global gravity field solutions (level-0 to level-2), followed by the generation of gridded level-3 time series of TWS variations. Subsequently, the gridded level-4 GWS variations are generated using the other compartments' storage data. The gridded data products are publicly available at GFZ's data portal GravIS (Gravity Information Service, `https://gravis.gfz.de`)[1].

All necessary information explaining the processing and the generation of the G3P data product are provided by Dahle et al. (2025) and Güntner et al. (2026). A more detailed

[1]GravIS is an online data portal that provides access to gravity-field–related data products, services, and visualizations derived from satellite gravimetry.

https://doi.org/10.5194/egusphere-2026-975
Preprint. Discussion started: 27 March 2026

explanation of level-0 to level-4 processing stages is also provided in Section S1 of the supplementary material to this paper. In the following, we highlight most important aspects of level-4 processing. GWS variations are derived from level-3 GRACE/GRACE-FO TWS anomalies using a water balance approach in which storage variations of other continental water compartments are subtracted from TWS (see, e.g., Frappart and Ramillien 2018 for an overview):

$$\mathrm{GWS} = \mathrm{TWS} - (\mathrm{RZSM} + \mathrm{SWE} + \mathrm{GM} + \mathrm{SWS}) \tag{1}$$

This approach is implemented in the G3P data product (Güntner et al., 2024, `https://www.g3p.eu/`), which we use in this study. For G3P, TWS is based on the level-2 spherical harmonics solution of the COST-G combination product (Jäggi et al., 2020; Meyer et al., 2023). The water storage compartments subtracted to estimate G3P GWS variations are:

i) **Root-zone soil moisture (RZSM):** Derived from a multi-satellite surface soil moisture product of the Copernicus Climate Change Service (C3S) with spatial-temporal gap filling and an infiltration approach to 2 m soil depth (Pasik et al., 2023; Preimesberger et al., 2025).

ii) **Snow water equivalent (SWE):** Satellite-based data from the GlobSnow product (Luojus et al., 2021) combined with the Copernicus Global Land Service (CGLS) operational SWE product and extended to global coverage for G3P.

iii) **Glacier mass change (GM):** Based on global gridded data from C3S (Dussaillant et al., 2023), further developed for G3P to monthly resolution (Zemp and Welty, 2023).

iv) **Surface water storage (SWS):** Storage in lakes, rivers, wetlands, and reservoirs from the OS LISFLOOD hydrological model as implemented in the Global Flood Awareness System (GloFAS) of the Copernicus Emergency Management Service (Choulga et al., 2024; Van Der Knijff et al., 2010).

To ensure consistency with the effective spatial resolution of GRACE-derived TWS (approximately 300–500 km), all monthly compartmental storage time series are spatially smoothed with a Gaussian filter of 250 km filter width prior to subtraction (Sharifi et al., 2025). The filtered storage data are then subtracted from TWS to obtain time series GWS variations (anomalies w.r.t. reference period). Measurement-type uncertainties are provided based on Merchant et al. (2017). For this study, uncertainties are calibrated from the data to optimally represent the combined effects of measurement noise and natural climate variability (cf. Section 2.2).

For each cell of the global grid, G3P delivers a time series of monthly water storage with units of equivalent water height as anomalies with respect to the reference period. The G3P V.1.12 dataset (Güntner et al., 2024), which we use in this study, is provided on a $0.5° \times 0.5°$ latitude-longitude grid (nominal resolution), though the effective resolution of GRACE/-FO observations is coarser (∼300–500km due to filtering; Dahle et al., 2025). Thus, to reduce computational load while preserving spatial coverage and important hydrological signals we downsampled the data by selecting every second grid cell, resulting in $1° \times 1°$ spacing. This yields 14,766 time series over the continents for each variable, ranging from April 2002 to September 2023 (except Antarctica and Greenland). With gaps, such as between end of GRACE and beginning of GRACE-FO, we have – for each grid cell – a time series of monthly resolution with 225 data points. Besides the focus variables TWS and GWS, we also processed the other compartmental storage variables. Certain compartments contain grid points with

https://doi.org/10.5194/egusphere-2026-975
Preprint. Discussion started: 27 March 2026

no contributions, as no effect is measurable in certain regions (e.g., glaciers, or SWE near the equator).

Regarding spatial resolution, a common problem of satellite gravimetry as realized by GRACE and GRACE-FO is the leakage effect (e.g., Dahle et al. 2025). Leakage describes the inability to localise signals in the GRACE-derived data sets exactly. The first cause of leakage is signal attenuation due to the distance between the signal source on, or close to, the Earth's surface and the observing satellites. Further data processing steps towards TWS data, foremost filtering, are further reducing the spatial resolution of TWS. Together, leakage leads to apparent signal loss (leakage out) or gain (leakage in) inside a given integration region. In our data analysis, we will refer to this when appropriate.

2.2. Methods

Each of the G3P time series analyzed is represented by $\mathbf{y}^T = [y(t_0), y(t_1), .., y(t_k), .., y(t_{n-1})]$, where the index $k = 0, 1, ..., n-1$ refers to the $k-$th of n samples in total, and t is the time (in days). Although GRACE/-FO monthly solutions are not evenly spaced due to irregular mission operations (e.g., see `https://grace.jpl.nasa.gov/data/grace-months/`, last accessed January 20, 2026), we follow common practice and take on-average monthly sampling ($\Delta t = 30.4375$ days), consistent with the average length of a Gregorian month. Observations refer to the middle of each month, and gaps are left as they are (e.g, GRACE to GRACE-FO). The following additive time series model is considered to explain each time series:

$$y(t_k) = a + b \cdot t_k + \sum_{j=1}^{m} (U_{j,1} \cos(2\pi f_j t_k) + U_{j,2} \sin(2\pi f_j t_k)) + z(t_k) \tag{2}$$

a and b are the intercept and slope of the linear trend function, $U_{j,1} = \bar{U}_j \cos(\varphi_j)$, $U_{j,2} = -\bar{U}_j \sin(\varphi_j)$, with $\bar{U}_j$ and φ_j being amplitude and phase of a number of m constant-amplitude periodic signals (at given frequencies f_j). Based on our pre-analysis of variables' power spectral densities (PSD) (Section 3.1), we choose $m = 6$, comprising the annual periodic signal (365.25 days), and the first five harmonics. These parameters represent the functional model. The residuals $z(t_k)$ are represented by the stochastic processes under consideration, and reflect inter- and intra-annual geophysical signals (as "climate noise") and sensor noise, represented by a combination of autocorrelated (persistent) and uncorrelated processes. For each time series and each variable, with an individual fit of Eq. (2), we estimate the functional model, as well as the stochastic processes as a combination of long/short-range memory and a white noise process. The observation covariance matrix $\mathbf{C_{yy}}$ is considered to be a combination of two different models to represent the stochastic variability of the time series (e.g., Montillet and Bos, 2019): Based on the findings of a literature review and the explorative data analysis (Section 3.1), we consider two different combinations of stochastic models:

$$\mathbf{C}_{\mathbf{yy}}^{(1)} = \sigma_{PL}^2 \cdot \mathbf{J}_{PL}(\kappa) + \sigma_{WN}^2 \cdot \mathbf{I} \tag{3}$$

$$\mathbf{C}_{\mathbf{yy}}^{(2)} = \sigma_{AR1}^2 \cdot \mathbf{J}_{AR1}(\phi) + \sigma_{WN}^2 \cdot \mathbf{I} \tag{4}$$

σ^2 is the variance component (amplitude) of the individual stochastic model, with its correlation structure represented by $\mathbf{J}$. The matrices in Eqs. (3) and (4) are of dimension $n \times n$. The superscript $^{(1)}$ stands for the power-law plus white noise PL+WN (PLWN) model. Superscript $^{(2)}$ stands for the autoregressive process of order 1 plus white noise AR1+WN (AR1WN) model. $\mathbf{I}$ is the identity matrix. The PLWN model is central and represents long-range memory processes, as observed in TWS and GWS from sustained precipitation or glacial melting, where variability persists over extended timescales. In contrast, the AR1WN

https://doi.org/10.5194/egusphere-2026-975
Preprint. Discussion started: 27 March 2026

model captures short-range memory processes, such as transient fluctuations in soil moisture or surface water driven by precipitation. For both colored-noise processes, we added white noise to account for uncorrelated noise effects, such as high-frequency measurement noise. $\mathbf{J}_{PL}$ depends on the spectral index κ (Bos et al., 2020), which represents, in a double-logarithmic plot, the linear slope characteristic to the PL PSD. At this stage, we recall that the random-walk (RW), the flicker-noise (FN), and the WN models are special cases of the PL model: κ = -2 is RW noise, κ = -1 is FN, and κ = 0 represents white noise. AR1 represents the autoregressive model of order 1 (e.g., Klos et al., 2018), and $\mathbf{J}_{AR1}$ depends on the lag-1 coefficient ϕ, and flattens out in the spectral domain for long periods (less correlation).

We exemplarily illustrate the different stochastic processes and noise types in Figure 1, left panel. These synthetic time series are sampled GRACE-like, with 225 samples and gaps as-is. All process realizations were drawn from the same normally distributed white driving noise. The corresponding PSDs (Figure 1, right panel), show that the processes reflect different correlation structures and strengths, particularly at low frequencies. The FN and RW noise realizations exhibit ever-increasing power at low frequencies, which strongly impacts the estimated trend uncertainties towards inflation. These effects diminish for short-range memory models, such as AR1. The white noise PSD has constant power along all frequencies and thus shows no correlations, which results in much lower trend uncertainty and, thus, narrower confidence intervals (too optimistic under the presence of colored noise, see, e.g., Mudelsee 2019). The higher the magnitudes in the long periods (low frequencies), the stronger the temporal correlation, and the higher the uncertainty of the estimated trends is.

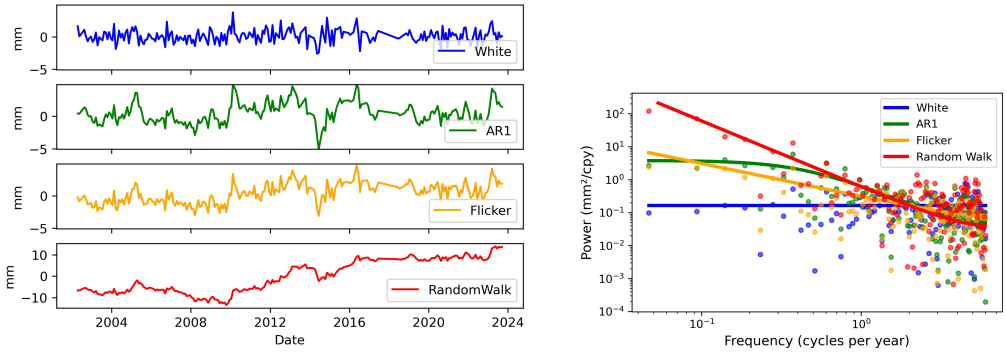

Figure 1: Left panel: synthetic GRACE-like time series for the stochastic processes under consideration: white noise, AR1 noise, flicker noise and random walk noise (note: different y axis limits for the random walk) (left panel). Right panel: power spectral densities (PSDs) for the stochastic processes shown in the left panel. Dots represent empirical power spectral densities.

We use the Hector software (Bos et al., 2008, 2021) to estimate the individual parameters of the functional model (Eq. 2) and the respective stochastic model choice (Eq. 3 or 4), for each time series of the grid. The model of Eq. 2 is linear and the parameter vector is defined by $\mathbf{x} = [a,\ b,\ \bar{U}_1 \cos(\varphi_1),\ -\bar{U}_1 \sin(\varphi_1), ...,\ \bar{U}_j \cos(\varphi_2),\ -\bar{U}_j \sin(\varphi_j)]^T$; we estimate the parameters using GLS, and the parameters of the stochastic processes are estimated using variance component estimation (e.g., Bos et al. 2020). The variance components for each model and the unknown parameters of the $\mathbf{J}_i$ matrices (Eqs. (3) and (4)) are estimated from the residuals of the parametric fit of Eq. (2) using Restricted Maximum Likelihood Estimation (RMLE) (Patterson and Thompson, 1971), which has, compared to conventional MLE, the ability to provide more realistic variance component estimates since it accounts for

https://doi.org/10.5194/egusphere-2026-975
Preprint. Discussion started: 27 March 2026

the loss of variance by the parameter fit (e.g., Gobron et al. 2022; Hohensinn et al. 2024). The parameters include the spectral indices and coefficients of the PL and AR1 models. The result, for each time series of the global grid, we estimate the 14 parameters in $\hat{\mathbf{x}}$, and the corresponding covariance matrix components $\mathbf{C}_{\hat{\mathbf{x}}\hat{\mathbf{x}}}$.

We use the following statistical significance test under the assumption of normally distributed residuals and parameters, and a two-sided confidence interval of 99%. We chose 99% to derive conservative change rates, under limited effect of false positives. To test if the estimated trend $\hat{b}$ from each TWS and GWS time series is significant, we define the null and alternative hypothesis by

$$H_0: \quad \mathrm{E}(\hat{b}) = 0 \tag{5}$$

$$H_A: \quad \mathrm{E}(\hat{b}) \neq 0 \tag{6}$$

For each time series and each variable, the test quantity can then be formed by (Amiri-Simkooei et al., 2019; Hohensinn et al., 2024)

$$T_b = \hat{b}/\sigma_{\hat{b}} \tag{7}$$

where $\sigma_{\hat{b}}$ is the 1-sigma standard deviation, reflecting the trend uncertainty, estimated through the parameter adjustment by $\sigma_{\hat{b}} = \sqrt{\mathbf{C}_{\hat{b}\hat{b}}}$, taken from the diagonal of $\mathbf{C}_{\hat{\mathbf{x}}\hat{\mathbf{x}}}$, which reflects the parameter variances. We use a two-sided confidence interval of 99%, which results in a threshold T_b=2.58.

For our explorative data analysis in Section 3.1, we further apply K-means clustering. K-means clustering is an unsupervised machine learning algorithm that partitions data into a predefined number of clusters by minimizing within-cluster variance. Applied to a time-series-populated feature matrix, it iteratively assigns the time series to the nearest cluster. It was introduced by MacQueen (1967) to develop a simple and efficient method for partitioning multivariate data into homogeneous groups.

To reliably quantify volumetric changes, the tables of continental water storage trends (TWS and GWS) in Section 3.3 were derived from G3P grid-cell time series and exhibit *statistically significant* trends only, which differs from earlier approaches. Each significant trend of a grid cell is assigned to a continent, and its surface area is computed geodetically (area-aware weighting). Continental water storage changes are computed by direct physical integration of significant grid-cell trends over continental areas,

$$\Delta V = \sum_i A_i \cdot b_i \cdot 10^{-6}, \tag{8}$$

where b_i denotes the grid-cell trend ($\mathrm{mm\,yr^{-1}}$ equivalent water height) and A_i the corresponding grid-cell area ($\mathrm{km^2}$). The factor 10^{-6} converts $\mathrm{mm\,km^2}$ to $\mathrm{km^3}$, yielding volume change rates in $\mathrm{km^3\,yr^{-1}}$, numerically equivalent to $\mathrm{Gt\,yr^{-1}}$ for freshwater. This approach preserves physical additivity and mass conservation, and allows separation of positive (gain) and negative (loss) contributions, whose algebraic sum defines the net balance. At the global level, global mean trends ($\mathrm{mm\,yr^{-1}}$) are reported as significant-area-weighted averages of continental values, while global volume changes are then obtained by summing continental volume contributions. The procedure is described in more detail in Section S2.

https://doi.org/10.5194/egusphere-2026-975
Preprint. Discussion started: 27 March 2026

3. Results

3.1. Analysis of Spatio-Temporal and Spectral Data Features

3.1.1. Time Domain Analysis

We first explore the spatio-temporal characteristics of TWS and GWS with respect to their trends and patterns at the global scale. Figure 2a shows dominant properties of the G3P TWS data, obtained from the K-means clustering, with the time series data as features, and by using 6 clusters. This grouping is solely based on the structural similarity of the time series, and does not yet include any information on trend estimates or their significance. A visual inspection reveals that globally most areas (covering large parts of North America, Asia, Africa, and Oceania) do not show long-term trends (cluster 0, purple, top-left time series), but are dominated by seasonal variations and interannual signals. Second to this, the blue cluster shows more pronounced seasonal variations, but also slightly negative trends (cluster 1, blue, top-middle time series), covering large regions of Western, Central, and South-Eastern Europe, the southwest of Asia and North America. This group also covers areas with considerable groundwater depletion due to agricultural activities (High Plains Aquifers and Central Valley in California, the Arab and Persian region, and North and East China). Regarding cluster 2 (turquoise, top-right time series), we observe further pronounced seasonal variations, but no strong trends, with regions located around the Tropical zone (e.g., West African Sudanian zone, northern South America, Central America, Central and South India). The strongest seasonal variations can be found in the Amazon Basin and the Zambesi in cluster 3 (green, bottom-left time series). Pronounced negative TWS trends as seen in cluster 4 (orange, middle-left time series) arise from surface water decline (Caspian Sea), groundwater depletion in northern India and around glacier and ice melting hotspots (e.g., Patagonia ice fields, the Canadian Arctic), while the hotspots of global TWS decline are the melting glaciers in the Gulf of Alaska and in the northern parts of Canadian Arctic Archipelago shown in cluster 5 (red, bottom-right time series panel).

https://doi.org/10.5194/egusphere-2026-975
Preprint. Discussion started: 27 March 2026

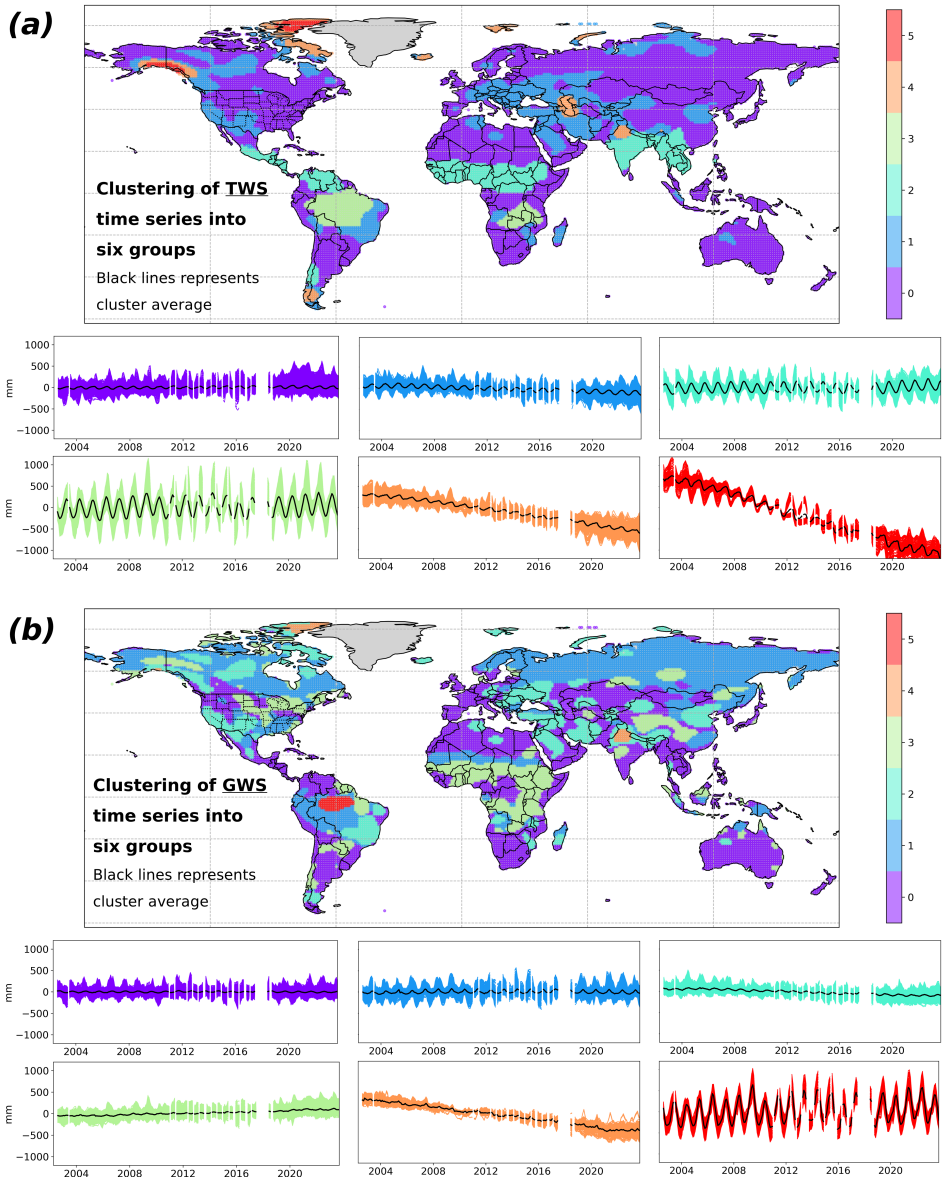

Figure 2: Overview on global trends in terrestrial water storage (TWS, panel a) and groundwater storage (GWS, panel b) variations, as seen from the G3P data. Grouping of similar time series using K-means clustering. The time series of the individual clusters are shown in six panels below the map using color-coded cluster IDs. The black curve represents the mean time series for each cluster. Units in millimeters of equivalent water height.

Figure 2b shows important spatio-temporal features of the G3P GWS data. Again, seasonal and interannual variations dominate most of the time series (clusters 0 and 1, purple and blue, top-left and top-middle time series), especially in the Northern hemisphere at high latitudes (blue cluster, top middle panel). The strongest seasonal variations are found in the center of the Amazon Basin, represented by cluster 5 (red, bottom-right time series), with peak-to-peak amplitude variations in equivalent water height of about 1000 millimeters.

https://doi.org/10.5194/egusphere-2026-975
Preprint. Discussion started: 27 March 2026

However, for GWS seasonal variations are less pronounced than for TWS because for the latter, RZSM is the dominant driver of seasonality. As a consequence, we can observe more subtle GWS trends: the turquoise cluster (cluster 2, top right) represents regions with moderate negtive GWS trends, covering large areas of Canada, the western and Southwestern U.S., central and eastern Europe, South America (Brazil), and several regions in Asia (including Arab Asia). The most pronounced negative GWS trends are found in the Canadian Arctic and Northern India (cluster 4, orange, bottom-middle time series panel). While the Indian GWS decline can clearly be attributed to groundwater pumping, the Arctic decline is questionable as it may be attributed to spurious leakage from Greenland ice mass loss , and potential modelling artefacts (see discussion further below). Several regions are characterized by positive GWS trends (cluster 3, green, bottom-left panel), e.g., around the U.S. Midwest and Great Lakes region, parts of Southern America (e.g., Upper La Plata Basin), Russia, Central China, and most clearly large parts of Central Africa. We further discuss the detectability and significance of trends in Section 3.3.

3.1.2. Spectral Analysis

To assess data characteristics in the spectral domain and to identify stochastic processes, we compute Lomb-Scargle periodograms for all time series and for each storage compartment. The resulting globally averaged PSDs (per-frequency) are shown in Figure 3, left panel. We observe significant peaks at the annual and semi-annual period, indicating the substantial contribution of seasons to water storage variations. Furthermore, peaks are at 3 and 4 cycles per year (cpy), i.e., at 4 to 3 month intervals, and additionally at 5 and 6 cpy (compartment variables), i.e., every 2nd month. When comparing to the synthetic examples presented in Figure 1, all variables show the presence of pronounced contributions of colored (correlated) noise (both of long and short-range type), following clear tendencies towards higher PSD magnitudes at low frequencies (long periods) and towards lower magnitudes at high frequencies (short periods). Note that presence of trends still slightly affects the PSDs at long periods.

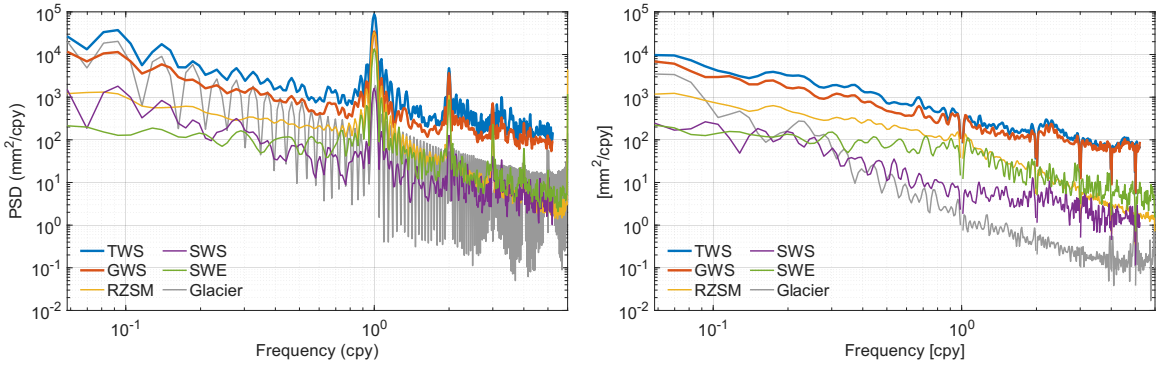

Figure 3: Averaged global power spectral densities (PSDs) of the G3P variables (left) and PSDs of the same variables after ordinary least squares (OLS) (TWS: Terrestrial Water Storage, GWS: Ground Water Storage, RZSM: Root Zone Soil Moisture, SWS: Surface Water Storage, SWE: Snow Water Equivalent, Glaciers).

To better assess this influence and to reveal the stochastic character of the data, we remove identified periodic seasonal signals (1-6 cpy) and a linear trend using ordinary least squares (OLS) regression. The resulting PSDs of the residuals (Figure 3, right panel) mostly reflect interannual variations and measurement system noise. For TWS, GWS, SWS, and glaciers, we observe spectra close to constant negative slopes (power-law behavior), indicating

https://doi.org/10.5194/egusphere-2026-975
Preprint. Discussion started: 27 March 2026

long-range dependence. Broad interannual (∼2–7 yr) power in TWS and GWS variations is largely explained by superposed climate modes: combinations of ENSO-/PDO-/AMO-related effects account for up 20% to 70% of interannual TWS variability in global basins, with interannual amplitudes of ∼10 cm equivalent water height (Pfeffer et al., 2022). The observed power-law spectra of GWS reflect long-memory GWS dynamics as confirmed by multi-decadal groundwater level records which exhibit fractal (power-law) scaling and long-range persistence (Li and Zhang, 2007; Little and Bloomfield, 2010).

The spectra of SWE and RZSM tend to flatten out at long periods, indicating AR1-type (short-range memory) behaviour. RZSM residuals are well described by AR1-type exponential memory, with slightly stronger persistence in drier regimes (Orth and Seneviratne, 2012). SWE anomalies exhibit strong within-season persistence, consistent with short-range memory behavior (Sospedra-Alfonso et al., 2016), which is also identifyable from our SWE spectrum, following a correlation structure of an AR1 process. In contrast, PSDs of glacier mass and SWS variations also indicate power-law behaviour. In line with SWS variations, long-range dependence with power-law behaviour was also shown for global river runoff (Koscielny-Bunde et al., 2006), as it also relates to components with longer memory such as groundwater and glaciers. Glacier mass anomalies can show power-law behaviour over the analysis band (e.g., 0.05–0.5 cpy) because multiple slow response times make glaciers a multi-timescale low-pass system. "A glacier can be thought of as acting as a low-pass spectral filter characterized by a red-noise-type power spectrum" (Roe, 2011), i.e., with stronger low-frequency correlation than an AR1 but still finite memory on very long timescales.

Remaining side lobes in the residual PSDs can be attributed to signals with time-variable amplitude. Furthermore, periods of seasonal variations are not exactly the same each year, and this variability could also introduce leakage-type behaviour, i.e., the broadened side lobes for RZSM, SWE, and also GWS around 1 cpy. Residual inter-harmonic power in GRACE/GRACE-FO TWS/GWS (e.g., 2-3 and 3-4 cpy) arises from cyclostationary seasonal amplitude and phase modulation – this mechanism has been explained in GRACE TWS through spectral characteristics of cyclostationary signals, where amplitude modulation of the annual cycle creates detectable sideband energy (Hamlington et al., 2019; Chandanpurkar et al., 2021). ENSO-driven interannual variability can also cause frequency modulation that affects these sidebands (Cheon et al., 2021). In addition, seasonal variability is not universally well represented by a small set of sinusoidal harmonics: in regions such as monsoon-dominated India, strongly asymmetric recharge–discharge cycles produce sawtooth-like seasonal signals, while parts of central Africa exhibit secondary seasonal peaks, both of which introduce higher-harmonic and inter-harmonic spectral power that cannot be fully captured by harmonic models. However, remaining effects can be considered to have little effect on the trend determination only, and are largely captured by the stochastic model calibration. In data records with gaps, spectral leakage further broadens lobes in these sidebands (Thomson, 1982). These patterns in TWS variability were identified as key targets for future satellite gravity missions (Jensen et al., 2020). From about 3-4 cycles-per-year (cpy) onwards, a white noise type contribution to the variables is seen, being identifiable as a flattening of the spectra.

A further inspection of globally averaged PSDs before and after removal of trends and seasonal components shows that low-frequency power is strongly influenced by trends in glaciers and, to a smaller extent, in SWS and TWS, whereas RZSM and SWE exhibit comparatively weak trend contributions. After detrending and de-seasonalization, the residual spectra reveal distinct stochastic characteristics across compartments, with long-memory behavior dominating TWS, GWS, SWS, and glacier mass, and short-range persistence prevailing in RZSM and SWE. Representative PSDs of GWS and RZSM (cf. Figure S1 in Section S3.1) further high-

https://doi.org/10.5194/egusphere-2026-975
Preprint. Discussion started: 27 March 2026

light this contrast, with RZSM dominated by seasonal to interannual variability (as dominant seasonal contributor) and GWS showing stronger low-frequency trend influence, as it is also inferred from the clustering time-domain analysis. While low-frequency power associated with trends is strongest in glaciers, SWS, and TWS, the interannual band lower than 1 cpy is largely dominated by GWS contributions to TWS (followed by RZSM), except at the very lowest frequencies where glacier signals prevail, and GWS remains the dominant contributor to TWS across most of the spectrum. In addition, the residual spectra reveal structured seasonal and cyclostationary behavior, particularly in GWS, with distinct spectral signatures persisting in the 2–4 cpy band after trend and periodic removal. More details of the spectral analyses are provided in Section S3.1.

3.1.3. Summary of Time- and Spectral-Domain Analysis

The time-domain clustering identifies spatially highly coherent regions of groundwater depletion and glacial mass loss (e.g., North America, India, Arctic regions), as well as emerging positive groundwater trends across parts of Africa and mid-latitude aquifers. TWS variations show high amplitudes of seasonal variations, which is less emphasized for GWS spectral characteristics, which are dominated by seasonal and interannual variability with pronounced low-frequency power. The literature-review-based analysis also underpins the advanced quality of G3P COST-G solutions, characterized by high signal-to-noise ratios and stable noise characteristics (Meyer et al., 2023).

Our spectral pre-analysis yields two key findings:

- *Low-frequency behavior and memory structure:* Globally averaged PSDs show that TWS low-frequency power is primarily controlled by trends (glaciers, SWS) and interannual effects (mostly driven by GWS variations), whereas RZSM and SWE exhibit comparatively weak trend contributions. Residual spectra indicate long-memory behavior for TWS, GWS, SWS, and Glacier, and short-range persistence for RZSM and SWE.

- *Contrasting variability regimes:* Representative PSDs of GWS and RZSM (Figure S1) highlight distinct variability regimes, with RZSM dominated by seasonal fluctuations and GWS showing a pronounced reduction of low-frequency power after detrending and strong long-memory persistence, which indicates sustained groundwater dynamics.

Based on this pre-analysis, we select PLWN models for TWS, GWS, SWS, and Glacier, and AR1WN models for RZSM and SWE regarding our trend quantification.

https://doi.org/10.5194/egusphere-2026-975
Preprint. Discussion started: 27 March 2026

3.2. Global Trends in TWS and GWS, and their Significance

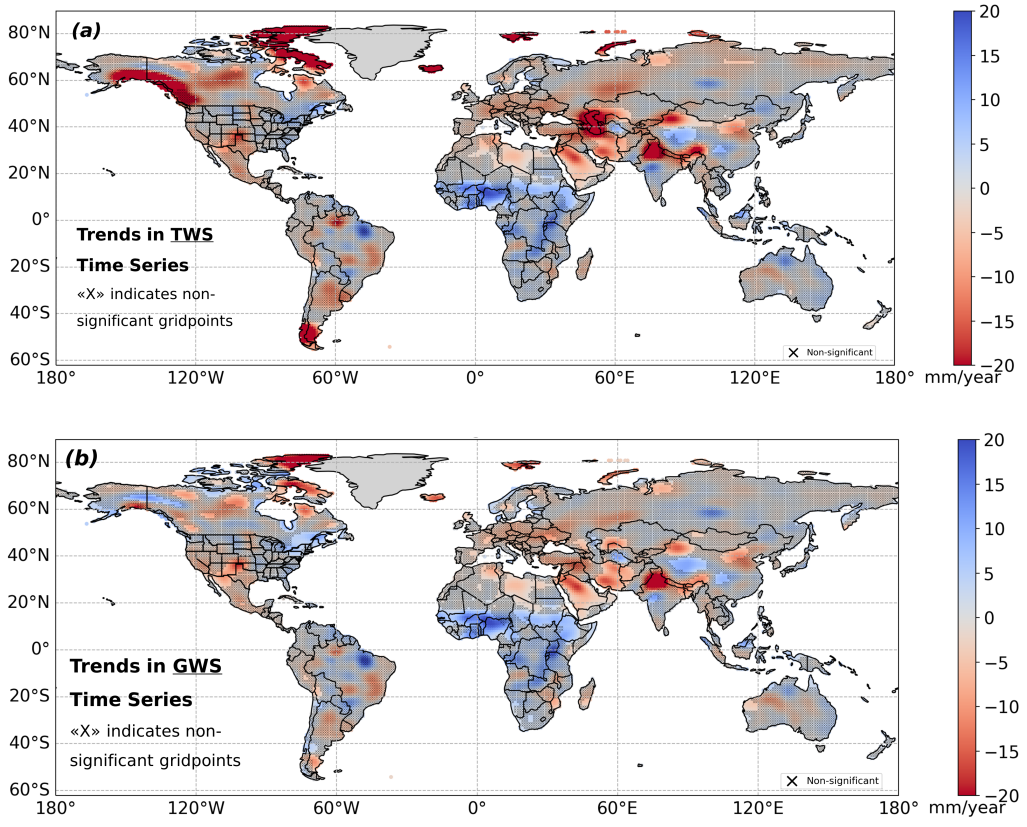

Figure 4: Significant G3P TWS (panel a) and GWS trends (panel b) under consideration of the calibrated time series models introduced in Section 2, and the statistical test. Shading with "X" represents data with insignificant trends, while all non-shaded trends represent statistically significant trends.

As explained in Section 2, we fit trends (alongside the other parameters) to each TWS and GWS grid-cell time series. For the stochastic component, we use PLWN as identified in Section 3.1. Along with the estimated trends, Figure 4 highlights the significant trends at the 99% confidence level in TWS (top) and GWS (bottom), and represents our main results; trends in G3P storage components (glacier mass, RZSM, SWS, SWE) are shown in Figure 5, for which also the identified stochastic processes have been fitted. Maps of estimated trends without shading can be found in Figures S3 and S4. The same figures, as well as Figure S5, also discuss stochastic properties and trend distributions of the TWS and GWS data.

Normality diagnostics are carried out for TWS and GWS (Figure S2), which constitute the primary targets of trend analysis in this study. This normality check is performed to show the reliability of our trends and trend uncertainties estimated from these data, when using the GLS estimator under serial autocorrelation.[2]

[2]For individual storage components, deviations from normality are expected (e.g., RZSM and SWE); however, when propagated into TWS and GWS, these deviations are not expected to strongly impact the interpretation of trends.

https://doi.org/10.5194/egusphere-2026-975
Preprint. Discussion started: 27 March 2026

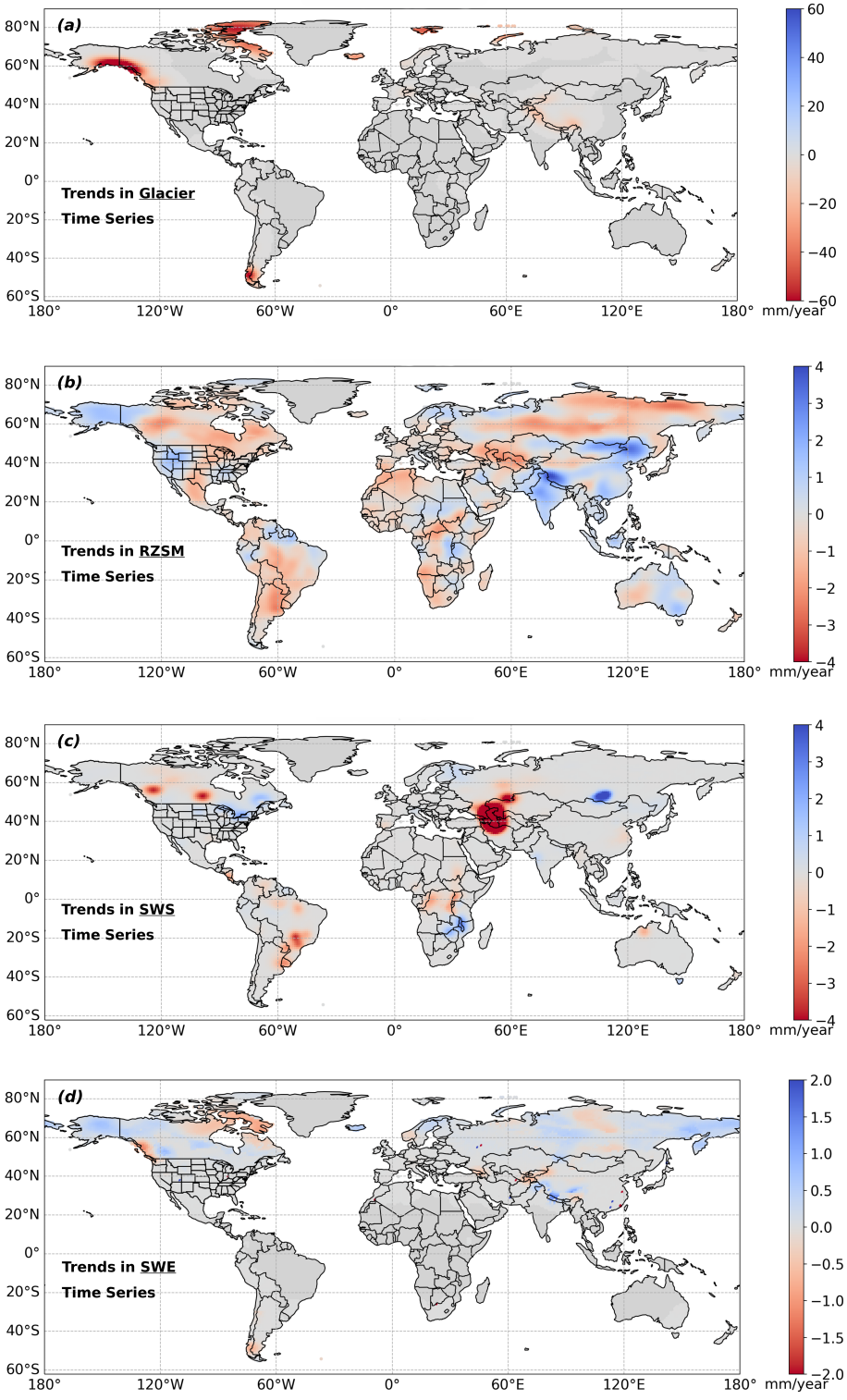

Figure 5: Global trends in Glacier (panel a), RZSM (panel b), SWS (panel c) and SWE (panel d).

https://doi.org/10.5194/egusphere-2026-975
Preprint. Discussion started: 27 March 2026

Major significant continental TWS trends coincide with regions of strong ice loss (Patagonia/Southern Andes, Alaska, Arctic islands) and are consistent with earlier work (Velicogna, 2009; Jacob et al., 2012; Wouters et al., 2019; Braun et al., 2019; Ciracì et al., 2020). In the G3P glacier component (Figure 5a), glacier retreat dominates low-frequency TWS decline in Canada, Alaska, the Arctic, Patagonia, and the Himalaya, reaching magnitudes up to ∼–100 mm/yr. GRACE-derived glacier mass budgets similarly show strongly negative trends in Alaska, Patagonia, Arctic Canada, Svalbard, and the Russian Arctic, and sum up to ∼199 km^3/yr over 2002–2016 (Wouters et al., 2019) (also excluding Greenland and Antarctica). Additional prominent negative TWS trends are associated with drought and water depletion, including regions with possible or partial direct human impact (Rodell et al., 2018), and long-term declines in the Aral and Caspian basins driven by irrigation diversion (Aral) or regional aridification and enhanced evaporation (Caspian). In the following, we analyze the TWS and GWS trends (Figure 4) for each continent individually, accompanied by a discussion of drivers and auxiliary parameters from the fitting process. More detailed discussions can be found in Section S3.2, which especially addresses the rather complex trend situation in Northern America.

3.2.1. North America

Strong TWS declines near the Gulf of Alaska and the Canadian Arctic Archipelago primarily reflect glacier/ice mass loss (Rodell et al., 2018; Wouters et al., 2019). Beside the glaciated regions, significant TWS/GWS declines in parts of the Mackenzie and Yukon basins are consistent with permafrost-thaw-related hydrological change, indicating towards groundwater connectivity/discharge and associated shifts in soil moisture and evapotranspiration (Lin et al., 2022; Wright et al., 2022). In the Alaska–Yukon region, GWS patterns should be interpreted cautiously because signal separation is challenging in glaciated and permafrost-dominated settings – coastal negative anomalies may reflect residual leakage from glacier mass loss, and differences to earlier GRACE-period results (Muskett and Romanovsky, 2011; Lin et al., 2022) may reflect time-period dependence and/or product and processing differences.

In the Canadian Prairies (Alberta; Saskatchewan River Basin), TWS declines are often not significant due to strong interannual variability, and are accompanied by large trend uncertainty (cf. Section S3.3, Figure S3), whereas GWS shows more robust significant declines in parts of the basin, consistent with groundwater extraction under semi-arid conditions and recurrent drought (Hamdi and Goïta, 2023; Wang et al., 2025). Western/central Canadian drying patterns are broadly consistent with independent GRACE-based assessments (Wang et al., 2025; Li and Rodell, 2024). In northern Quebec and the Hudson Bay region, our analysis indicates drying, which is consistent with recent evidence for a transition toward widespread northern Canadian drying and permafrost-driven storage losses (Li et al., 2016; Chandanpurkar et al., 2025; Huang et al., 2025; Wang et al., 2025), noting that Glacial Isostatic Adjustment (GIA) model uncertainty (cf. Section 3.2.7) can affect trend magnitudes.

In the Great Lakes Basin, positive TWS tendencies are consistent with the observed 2013–2017 transition from record lows to record highs (Gronewold and Rood, 2019), while corresponding GWS trends are weak in our data, and differences to earlier shorter-period analyses (Huang et al., 2012) may reflect the longer time span available for this analysis. In eastern Canada, localized significant positive TWS/GWS trends likely reflect increased precipitation and recharge (Dubois et al., 2022), while differences to other products or periods (Fatolazadeh and Goïta, 2021) may reflect resolution, end year, or GIA/signal-processing choices. Apparent GWS declines in the High Arctic (Queen Elizabeth Islands) require caution due to potential leakage from Greenland, GIA model errors or imperfections in the compartment components.

https://doi.org/10.5194/egusphere-2026-975
Preprint. Discussion started: 27 March 2026

Component trends support our interpretations: SWE shows negative trends in southwestern Canada and the Pacific Northwest (Figure 5d); SWS exhibits basin-scale anomalies (e.g., Williston Lake; Lake Winnipeg; Great Lakes) which shows to be consistent with regulation and lake-level variability (Shrestha et al., 2012; Beltaos and Peters, 2024; Kayastha et al., 2022); and RZSM indicates widespread drying in central and western Canada, which is consistent with precipitation-regime changes and permafrost thaw impacts (Rodell et al., 2018; Li et al., 2016; Bonsal et al., 2019; Li and Wang, 2022).

Regarding the USA and northern Mexico, significant TWS and GWS declines occur across the southwestern US (including New Mexico and Arizona) and the High Plains Aquifer, extending into northern Mexico; GWS also declines near Mexico City. These patterns are consistent with groundwater depletion for irrigation, and were intensified during recurrent droughts (Scanlon et al., 2012; Konikow, 2015; Jasechko et al., 2024), with depletion in the High Plains Aquifer exceeding –20 mm/yr in our results (Haacker et al., 2016). Component trends show limited large-scale SWE/SWS contributions over the US, while RZSM trends confirm drought impacts across the Midwest and into northern Mexico (Figure 5).

3.2.2. South America

Apart from Patagonia ice-mass loss (Tapley et al., 2019; Rodell et al., 2018), we observe significant TWS/GWS declines in the Altiplano, with negative GWS trends (down to ∼–100 mm/yr) consistent with reports of groundwater decline from agricultural extraction and mining activity (Gonzales et al., 2025; Hernández et al., 2021; Kirshen et al., 2025). In the Andean "Lithium Triangle", brine/groundwater extraction also contribute to declines under limited recharge (5–30 mm/yr) (Kirshen et al., 2025). Localized low-magnitude positive GWS trends near the northern Argentina–southern Bolivia–northeastern Chile triangle may reflect recharge variability, while spatially offset Patagonia GWS trends (northwestern Chubut positive; northeastern Santa Cruz negative) show limited correlation with the glacier component, which suggests the presence of non-ice-related hydrologic signals.

Across South America, many TWS/GWS trends remain non-significant due to strong interannual variability (PL κ approaching random-walk; Section S3.3). In the Amazon Basin, trends show dipole-like spatial structure (negative in the north; positive near the Delta) but are not significant; basin-mean tendencies remain broadly consistent with reported storage gains, while strong ENSO events and recovery periods contribute to variability (Rodell et al., 2018; Chaudhari et al., 2019; Satizábal-Alarcón et al., 2024; Chandanpurkar et al., 2025). In the southern La Plata region, drought-related declines reported for 2002–2009 (Chen et al., 2010) do not remain significant over 2002–2023, which is consistent with episodic drought and recovery (Naumann et al., 2022) events. Similarly, in the São Francisco basin, reported depletion rates can still be masked by interannual variability, although there is evidence for streamflow reductions related to reduced groundwater discharge (Lucas et al., 2021; de Melo and Wendland, 2020).

In sub-components (Figure 5), RZSM shows negative trends across central South America (Bolivia, northeastern Argentina, Uruguay, Paraguay, southern/southwestern Brazil). While projections suggest increasing soil moisture in southeastern South America (Saito et al., 2025; Lai et al., 2023), our results indicate a recent historical decline; partly decreasing RZSM trends have also been reported from satellite and reanalysis products (Hirschi et al., 2025). SWS shows negative trends in the broader São Francisco region and around Uruguay/Paraguay, consistent with drought episodes and agricultural intensification (Chen et al., 2010; Naumann et al., 2022).

https://doi.org/10.5194/egusphere-2026-975
Preprint. Discussion started: 27 March 2026

3.2.3. Europe

Across Europe, TWS trends are generally spatially coherent and of moderate negative magnitude, with significant negative trends concentrated in southern Scandinavia and the northern UK, broadly consistent with GRACE-based continental assessments (Xanke and Liesch, 2022). A negative trend in southern Scandinavia may indicate a reversal relative to earlier reported 2002–2011 wetting (Wang et al., 2013), while northern UK trends are less documented in GRACE syntheses but there is alignment with in-situ groundwater declines (Jackson et al., 2015). For GWS, significant negative trends occur in eastern France, southern Ukraine, and northeastern Spain, consistent with Euro-Mediterranean depletion zones (Xanke and Liesch, 2022), while novel positive GWS trends in Denmark, coastal southwestern Finland, Estonia, and coastal western Norway may reflect increased recharge.

Component trends show weak-to-moderate RZSM drying over Iberia consistent with enhanced evapotranspiration (Spinoni et al., 2016), near-neutral SWS, small SWE tendencies (northward positives, southward negatives), and negative glacier trends over Norway and the Alps consistent with accelerated glacier mass loss (Zemp et al., 2019; Ciracì et al., 2020). In GIA-affected regions (Fennoscandia, British Isles, Canada), trend magnitudes and locally signs remain sensitive to uncertainty in the GIA correction.

3.2.4. Africa

Earlier studies emphasize natural variability in African TWS (Rodell et al., 2018; Ni et al., 2018). Our 2002–2023 analysis identifies statistically significant, but moderate magnitude declines across northern Africa (Algeria/Tunisia/Libya/northern Chad/northern Egypt) – depletion of NSAS/NWSAS isconsistent with GRACE-based assessments and attribution primarily to groundwater pumping, with mixed atmospheric-flux contributions for NWSAS (Wada et al., 2012; Goncalves et al., 2013; Frappart, 2020; Springer et al., 2023; Shalby et al., 2023). Generally, our patterns are consistent with the high-resolution GRACE trend map of Kvas et al. (2024).

In West Africa, pronounced significant positive TWS/GWS trends (often $> +20$ mm/yr) are concentrated in the Niger Basin and align with reported Sahelian groundwater increases and the "Sahelian paradox" (recharge enhancement linked to land-use change) (Werth et al., 2017; Leduc et al., 2001; Favreau et al., 2009; Felfelani et al., 2017; Ahmed and Wiese, 2019; Springer et al., 2023). Central Africa shows a higher spatial heterogeneity: non-significant negative tendencies around parts of the Congo River and significant positive trends around Chad/Cameroon are affected from climate-mode influences (IOD/ENSO) and dominant subsurface contributions to basin storage (Felfelani et al., 2017; Jiang et al., 2021; Jarugula and McPhaden, 2023; Moihamette et al., 2024; Ahmed and Wiese, 2019; Springer et al., 2023). In East Africa, significant positive trends are concentrated in the northern Rift region (southern Sudan/Ethiopia/Somalia), while strong interannual variability limits robust detection further south (Boergens et al., 2024b; Anyah et al., 2018; MacDonald et al., 2012). Southern Africa shows general wetting tendencies with localized GWS declines (e.g., southern Mozambique, Madagascar) consistent with reported drought conditions (Hoell et al., 2017; Spinoni et al., 2014).

Across Africa, TWS variations are largely governed by GWS fluctuations (cf. Figures S3 and S4, panel 1). Component trends show RZSM drying in northwest Africa consistent with Mediterranean precipitation declines and increased drought frequency (Schilling et al., 2020; Hirschi et al., 2025), drying tendencies in parts of central Africa requiring further investigation, and southern Angola/Namibia drying consistent with projections and satellite evidence (Cook et al., 2020; Hirschi et al., 2025). SWS shows negative trends in the Lake Tanganyika/Lake Victoria regions and along the Congo River, while Lake Malawi shows

https://doi.org/10.5194/egusphere-2026-975
Preprint. Discussion started: 27 March 2026

positive tendencies which is in agreement with recent lake-level increases (Gbetkom et al., 2024).

3.2.5. Asia

Southwest Asia (Arab–Persian region): Significant GWS losses of ∼–8 to –10 mm/yr (with hotspots < −20 mm/yr) are consistent with GRACE-based evidence for groundwater depletion and reservoir regulation (Joodaki et al., 2014; Nikraftar et al., 2024) – losses are primarily linked to irrigation-driven over-extraction under limited recharge.

Central Asia (Caspian and Aral Sea basins): Caspian Sea decline is consistent with increased evaporation and aridification (Chen et al., 2017). Aral losses reflect long-term irrigation effects under drying climate conditions (Wang et al., 2018). Significant negative GWS trends around the Aral Sea (to ∼–12 mm/yr) may reflect irrigation-driven depletion and/or artifacts from SWS separation, which requires further investigation.

South Asia (Indian subcontinent): Northern India is a dominant Asian hotspot of TWS/GWS loss (to ∼–40 mm/yr) resulting from unsustainable irrigation pumping (Rodell et al., 2009; Dangar et al., 2021). In contrast, positive GWS trends (∼+10 mm/yr) near Surat (Gujarat) and eastward align with reported replenishment linked to management interventions (Bhanja et al., 2017; Asoka et al., 2017).

East Asia (China): Negative trends over the North China Plain/Northeast China are resulting from over-abstraction supported by wells, modeling, and geodetic observations (Feng et al., 2013b; Cao et al., 2013; Zhao et al., 2019; Gong et al., 2018; Zhong et al., 2023). The observed reductions in Xinjiang and the Tarim Basin are primarily driven by intensive water extraction in this hyper-arid region (Zhao and Li, 2017), while Yunnan/SW China negative trends align with drought linked to climate variability (Tang et al., 2014). Positive trends in the Yangtze/Sichuan Basin and parts of the Tibetan Plateau are consistent with precipitation/recharge and reservoir effects (Yao et al., 2016; Cui et al., 2022; Wang et al., 2011).

Northern Asia (Russia and Arctic): Significant negative TWS/GWS trends over Taymyr and adjacent Kara Sea regions are consistent with permafrost-thaw impacts on subsurface storage (Walvoord et al., 2012). More broadly, northern Russia shows weak-to-moderate drying patterns, often not significant, so these localized signals require continued monitoring.

Component trends across Asia show RZSM drying in the Caspian–Aral region (Chen et al., 2017; Singh et al., 2012; Wang et al., 2018), wetting in northern India and northeast China (possibly reflecting irrigation return flow and greening) (Piao et al., 2020), and extensive RZSM drying across northern Russian tundra/taiga requiring validation with independent products (Bring et al., 2016; Chandanpurkar et al., 2025). SWS declines around the Caspian and Aral confirm documented losses (Chen et al., 2017; Singh et al., 2012; Wang et al., 2018; Micklin, 2016); SWE shows broad positive Siberian tendencies despite decreasing snow-cover extent (Bulygina et al., 2011), with negative SWE trends in the Caucasus and Central Asian mountains (Shahgedanova et al., 2020). Section S3.3 (PL κ and trend uncertainties) indicates elevated interannual variability in selected Asian hotspots (e.g., Central Asia, Middle East, parts of China).

3.2.6. Oceania/Australia

GRACE-based analyses show a wet–dry contrast across Australia, with repeated gains in the tropical north/northeast and persistent deficits over western and southern regions (Yang et al., 2020). Our component analysis indicates a mild but significant GWS decline in central-west Western Australia, consistent with GRACE–model fusion studies showing groundwater-dominated long-term TWS reductions and rainfall deficits (Yang et al., 2020;

https://doi.org/10.5194/egusphere-2026-975
Preprint. Discussion started: 27 March 2026

Tangdamrongsub et al., 2017). Interannual variability, particularly in northern Australia, is strongly precipitation-driven; GRACE-derived TWS anomalies are tightly linked to vegetation anomalies (Yang et al., 2014). Long-term depletion in semi-arid, recharge-limited regions is consistent with global groundwater assessments (Döll et al., 2014).

3.2.7. The Role of Glacial Isostatic Adjustment (GIA)

GIA represents an important source of systematic uncertainty in GRACE/-FO trend analyses, particularly in formerly glaciated regions. Using an ensemble-based framework, Eicker et al. (2024) demonstrate that in parts of North America and Fennoscandia the magnitude – and in some localized cases also the sign – of GRACE-derived TWS trends can depend on the adopted GIA realization. The strongest sensitivities occur in the region around Hudson Bay and northern Quebec, where GIA gravity-rate signals are large and rather heterogeneous, and GIA-related uncertainty can locally exceed several $\mathrm{cm\,yr^{-1}}$ equivalent water height.

These regions coincide with areas highlighted in our analysis as requiring cautious interpretation, including northern Canada, parts of the Canadian Arctic Archipelago, Fennoscandia, and the British Isles. Importantly, however, Eicker et al. (2024) also show that over large parts of Europe and mid-latitude regions, hydrological trend estimates are comparatively robust with respect to GIA uncertainty. This supports the GIA-related stability of most of the continental-scale trends identified in our study.

As G3P GWS is derived from TWS, any residual GIA signal in TWS propagates directly into GWS trends. As a consequence, in strongly GIA-affected regions, apparent GWS trends may be biased at the level of several $\mathrm{mm\,yr^{-1}}$ locally, which potentially affects trend significance near detection thresholds. For this reason, we recommend to interpret GWS trends in the principal GIA regions with particular care, however, we emphasize that large-scale continental interpretations discussed in this study are plausible and are broadly consistent with literature.

3.2.8. Rates-of-Change, 95% Threshold and Summary

We present continentally aggregated mean trends and associated volume changes derived from G3P grid-cell time series that exhibit statistically significant trends, as explained in Section 2.2. Strong negative GWS trends over the northeastern Canadian Arctic Archipelago are likely affected by leakage and model limitations; this region is therefore excluded from the GWS table analysis.

For TWS, the global volume balance of all grid cells with significant trends amounts to $-145\ \mathrm{km^3\,yr^{-1}}$ (Table 1), dominated by losses in Asia ($-86.5\ \mathrm{km^3\,yr^{-1}}$) and North America ($-52.0\ \mathrm{km^3\,yr^{-1}}$), with smaller contributions from Europe ($-15.9\ \mathrm{km^3\,yr^{-1}}$) and South America ($-16.8\ \mathrm{km^3\,yr^{-1}}$), while notably affected by gains in Africa ($+25.9\ \mathrm{km^3\,yr^{-1}}$).

The global GWS volume balance is $-26.5\ \mathrm{km^3\,yr^{-1}}$ (Table 2), driven primarily by losses in Asia ($-54.5\ \mathrm{km^3\,yr^{-1}}$), with moderate losses in Europe ($-4.7\ \mathrm{km^3\,yr^{-1}}$) and North America[3] ($-3.9\ \mathrm{km^3\,yr^{-1}}$), and gains in Africa ($+37.2\ \mathrm{km^3\,yr^{-1}}$). Global groundwater losses, mostly driven by depletion, exceed $-100\ \mathrm{km^3\,yr^{-1}}$.

Our analysis of 2002–2023 G3P TWS and GWS trends reveals pronounced regional contrasts in continental water storage dynamics. The global TWS balance of $-145\ \mathrm{km^3/yr^{-1}}$ is consistent with earlier GRACE-based assessments documenting large-scale intensification of the terrestrial water cycle (e.g., Wouters et al. 2019; Rodell et al. 2018). In contrast, the GWS component shows substantially different continental contributions, with net groundwater changes accounting for about 18% of the continental TWS balance, but exhibiting strong

[3]The ice-sheet-covered part of the Canadian Arctic Archipelago is excluded due to known GWS artifacts.

https://doi.org/10.5194/egusphere-2026-975
Preprint. Discussion started: 27 March 2026

Table 1: TWS trend statistics by continent. Significant trends: $|\text{trend}|/\sigma \geq 2.58$ (99% confidence level). Mean trend: area-weighted mean. Volume totals: direct physical sum of $\sum A_i \cdot T_i \cdot 10^{-6}$. Global trend: significant-area-weighted mean.

Region	Areal Coverage			Volume Change (km^3/yr)			
	Area (10^6 km^2)	Sig. Area (10^6 km^2)	Sig. Frac.	Trend (mm/yr)	Gain (km^3/yr)	Loss (km^3/yr)	V (km^3/yr)
Africa	29.9	6.5	0.2	4.0	33.8	8.0	25.9
Asia	31.5	8.7	0.3	-10.0	8.7	95.2	-86.5
Europe	22.9	1.2	0.1	-13.7	0.9	16.8	-15.9
North America	21.2	2.9	0.1	-17.9	4.5	56.5	-52.0
Oceania	8.4	0.3	0.0	1.3	0.6	0.2	0.4
South America	17.6	0.8	0.0	-19.8	0.1	16.9	-16.8
Global	**131.5**	**20.4**	**0.2**	**-7.1**	**48.7**	**193.6**	**-144.9**

Table 2: GWS trend statistics by continent. Significant trends: $|\text{trend}|/\sigma \geq 2.58$ (99% confidence level). Mean trend: area-weighted mean. Volume totals: direct physical sum of $\sum A_i \cdot T_i \cdot 10^{-6}$. Global trend: significant-area-weighted mean.

Region	Areal Coverage			Volume Change (km^3/yr)			
	Area (10^6 km^2)	Sig. Area (10^6 km^2)	Sig. Frac.	Trend (mm/yr)	Gain (km^3/yr)	Loss (km^3/yr)	V (km^3/yr)
Africa	29.9	8.8	0.3	4.2	46.1	8.9	37.2
Asia	31.5	8.5	0.3	-6.4	12.5	67.0	-54.5
Europe	22.9	1.5	0.1	-3.1	1.9	6.6	-4.7
North America	21.2	4.5	0.2	-0.9	14.0	17.8	-3.9
Oceania	8.4	0.6	0.1	0.2	0.9	0.8	0.2
South America	17.6	0.8	0.0	-0.9	1.4	2.1	-0.7
Global	**131.5**	**24.7**	**0.2**	**-1.1**	**76.7**	**103.2**	**-26.5**

https://doi.org/10.5194/egusphere-2026-975
Preprint. Discussion started: 27 March 2026

regional variability. Groundwater depletion dominates water losses in (approximately 63% of the TWS decline there), remains a secondary contributor in North America (∼8%), and shows net gains in Africa that partly compensate surface-water and soil-moisture losses. Greenland and Antarctica are excluded from the analysis. Our net global groundwater storage decline of $-26.5\ \mathrm{km^3\,yr^{-1}}$ corresponds to ∼18% of the continental TWS loss ($-145\ \mathrm{km^3\,yr^{-1}}$). However, this net value contains substantial compensating groundwater gains in Africa. The gross groundwater loss ($\sim 105\ \mathrm{km^3\,yr^{-1}}$), is comparable to earlier model-based estimates (100–150 $\mathrm{km^3\,yr^{-1}}$; Döll et al. 2014) of depletion and accounts for approximately 53% of total gross continental water losses (103.2 of 193.6 $\mathrm{km^3\,yr^{-1}}$) – which is consistent with recent findings that groundwater dominates drying trends in non-glaciated continental regions, although about 15% less than reported by (Chandanpurkar et al., 2025). Thus, the relative contribution of groundwater to total TWS change strongly depends on whether global net budgets or drying-dominated continental regions are considered.

In **North America**, the continental TWS decline of about $-52\ \mathrm{km^3\,yr^{-1}}$ is dominated by cryospheric losses, particularly in Alaska and Arctic regions. Groundwater depletion is localized, most prominently in the High Plains Aquifer and parts of the southwestern United States and northern Mexico, while California's Central Valley does not exhibit a significant long-term GWS trend over the extended study period. Across Canada, hydrological changes are influenced by permafrost thaw and climate variability, with several Arctic signals requiring cautious interpretation due to known leakage and model limitations.

South America experiences moderate TWS losses of approximately $-17\ \mathrm{km^3\,yr^{-1}}$, largely driven by Patagonian ice mass loss, while groundwater contributes only marginally to continental totals. Localized GWS depletion associated with mining and irrigation is evident in the Altiplano, whereas much of the Amazon Basin shows strong interannual variability that masks trend significance.

Europe exhibits spatially coherent but moderate TWS declines ($\sim -16\ \mathrm{km^3\,yr^{-1}}$), accompanied by glacier retreat in alpine regions. Groundwater depletion is evident in parts of southern and eastern Europe, while northern regions show mixed signals influenced by precipitation variability and GIA uncertainties in the North.

Africa stands out with positive continental balances for both TWS ($+26\ \mathrm{km^3\,yr^{-1}}$) and GWS ($+37\ \mathrm{km^3\,yr^{-1}}$), reflecting widespread groundwater recharge in the West African Sahel that compensate depletion in North African aquifers. Climate-driven precipitation variability linked to large-scale modes strongly influences East and Central African water storage patterns.

Asia accounts for the largest share of global TWS losses ($-87\ \mathrm{km^3\,yr^{-1}}$), with groundwater depletion ($-55\ \mathrm{km^3\,yr^{-1}}$) representing the dominant contribution. Major hotspots are northern India, the Arab–Persian region, and the North China Plain, while positive GWS trends are associated with water management and reservoir operations are evident in parts of western India and the Yangtze Basin. High-latitude regions of northern Asia show emerging negative signals, which are potentially linked to permafrost and evapotranspiration changes.

Oceania shows a strong wetting-drying contrast, driven by ENSO variability, with persistent TWS declines in western Australia and localized groundwater declines consistent with regional water stress.

We have also repeated our water change analysis at a 95% confidence level (1.96 test threshold, Figure S6), which essentially leaves the large-scale groundwater storage patterns and implications unchanged, but reveals that several significant-trend-adjacent regions (e.g., over Europe) are exceeding the detection threshold for negative trends, which suggest emerging drying tendencies that are not statistically detectable at the 99% level. Likewise, regarding the volumetric changes, using a 95% significance threshold indicates that the principal

https://doi.org/10.5194/egusphere-2026-975
Preprint. Discussion started: 27 March 2026

conclusions from the 99% analysis basically remain unaffected (see Tables S1 and S2): The global continental TWS net loss increases moderately from −145 to −161 $km^3\,yr^{-1}$, while total gross continental TWS losses rise from 194 to 226 $km^3\,yr^{-1}$. Similarly, net GWS decline goes from −26.5 to −31.4 $km^3\,yr^{-1}$, and gross groundwater depletion increases from 103 to 129 $km^3\,yr^{-1}$. Importantly, the relative contribution of groundwater to total continental water loss changes only marginally: GWS accounts for ∼18% (99%) versus ∼20% (95%) of the net TWS decline, and for approximately 53% versus 57% of total gross continental water losses.

Overall, while the sign and spatial distribution of continental water storage changes are robust, the effect of several mechanisms – particularly in GIA-affected regions – remain uncertain and need further investigation. This includes an improved treatment of GIA and further independent validation with complementary geodetic and hydrological observations. As discussed, we also see a need to further analyze the attribution of driving mechanisms to GWS trends, however, this is beyond the scope of this work.

3.3. Assessment of trend significance and model evaluation

To provide a more detailed assessment of trend significance, Figure 6 shows, for each GWS time-series cluster identified in Figure 2b, the scatter of trend magnitude to trend standard deviation. Gray shaded regions indicate statistically significant trends; a logarithmic scale is used for clarity. As already suggested by Figure 2a, the purple and blue clusters (clusters 0 and 1) dominate globally and are largely characterized by insignificant trends (Figure 6, top panels). This also applies to cluster 5 (red), covering much of the Amazon Basin, where strong seasonal and interannual variability leads to large trend uncertainties (bottom right panel). In contrast, cluster 4 (orange, bottom middle panel), mainly representing Arctic regions and India, is dominated by significant negative trends with comparatively small scatter. Cluster 3 (green, bottom left panel) is characterized by widespread groundwater increases across multiple continents, with approximately half of the trends reaching significance.

Figure 6: Analysis of GWS trend significance for each cluster of Figure 3. Dots represent trend magnitude versus trend standard deviation for each grid cell (a logarithmic scale is used for clarity).

To further investigate the separation between significant and non-significant trends, we focus on GWS cluster 2 (turquoise; top right panel of Figure 6), which contains comparable

https://doi.org/10.5194/egusphere-2026-975
Preprint. Discussion started: 27 March 2026

numbers of significant and non-significant time series. Similar to cluster 3, this cluster exhibits structured trend magnitudes, but with larger scatter in trend uncertainty driven by interannual variability. Figure 7a shows the spatial distribution of cluster 2, with crosses marking time series with non-significant trends. The cluster predominantly comprises small to moderate negative GWS trends, making it well suited for evaluating the sensitivity of the significance detection.

We further sub-cluster the cluster 2 time series using K-means, based on trend significance (binary), geographic latitude and longitude (demeaned), with all features standardized. Optimally interpretable results were obtained with seven sub-clusters. The resulting spatial separation of significant and non-significant series is shown in Figure 7b, and the corresponding time series are presented in Figure 8. In each panel, the upper time series shows the observations (with, for better visual clarity, periodic signals removed), while the lower panel shows residuals from the parametric model fit.

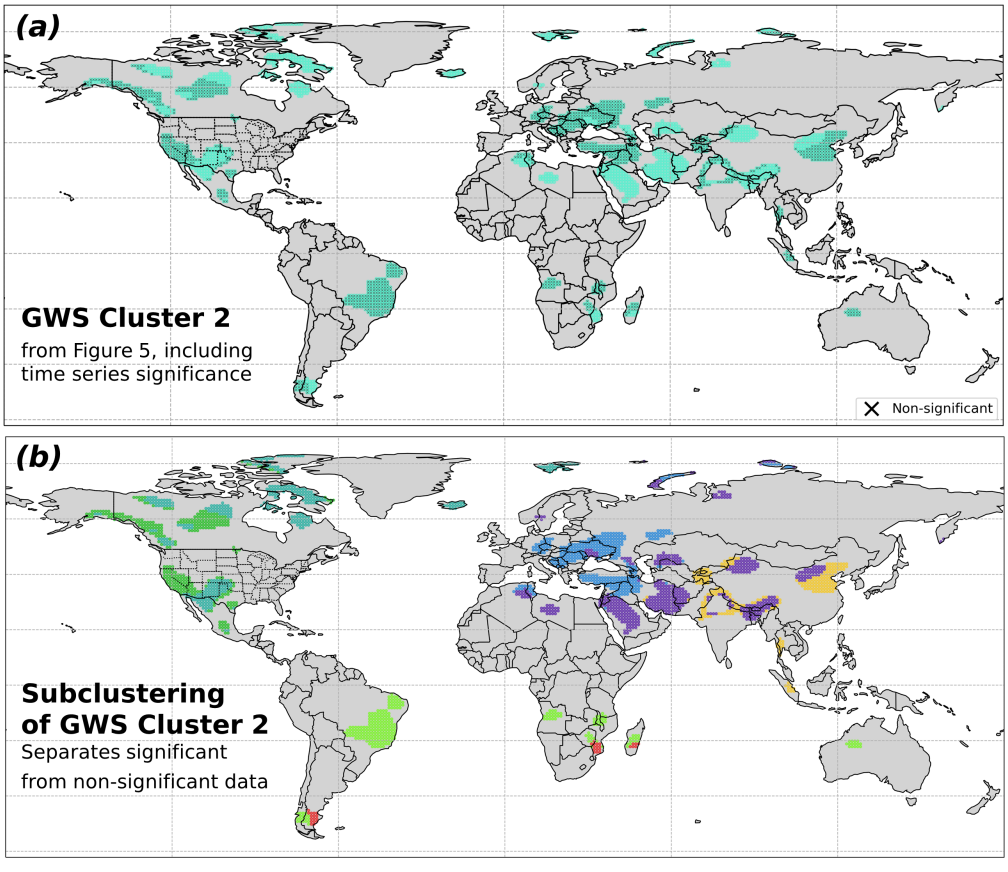

Figure 7: Panel (a): Spatial distribution of GWS cluster 2 from Figure 2b; crosses indicate time series with non-significant trends. Panel (b): Sub-clustering results using trend significance and geographic location as features.

https://doi.org/10.5194/egusphere-2026-975
Preprint. Discussion started: 27 March 2026

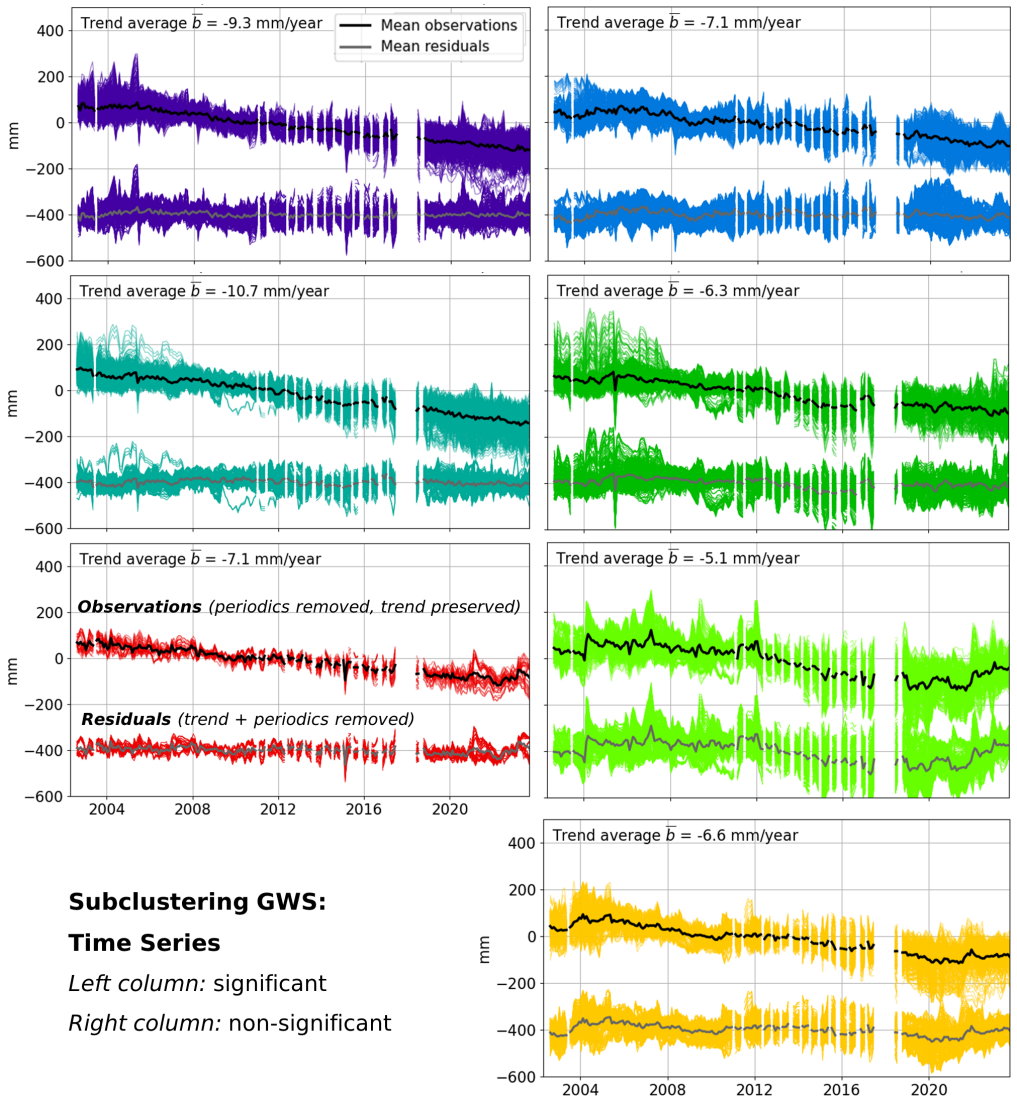

Figure 8: Time series corresponding to the sub-clustering of GWS cluster 2 (Figure 7b). Left panels show significant sub-clusters; right panels show non-significant ones. Observations (top) and residuals (bottom) are shown for each case.

Comparison of the significant (left column) and non-significant (right column) time series in Figure 8 reveals systematic differences. Significant trends range from approximately -7.1 to -11 mm yr^{-1}, whereas non-significant trends are weaker (-5.1 to -7.1 mm yr^{-1}). Residuals of significant series exhibit less scatter, while non-significant series show stronger interannual variability that obscures linear trends. In several cases, the mean residual signal dominates over the linear component, and some time series display weak non-linear behaviour, such as slight positive tendencies before 2007. Although such differences are subtle, it demonstrates the feasibility of the applied significance detection framework.

https://doi.org/10.5194/egusphere-2026-975
Preprint. Discussion started: 27 March 2026

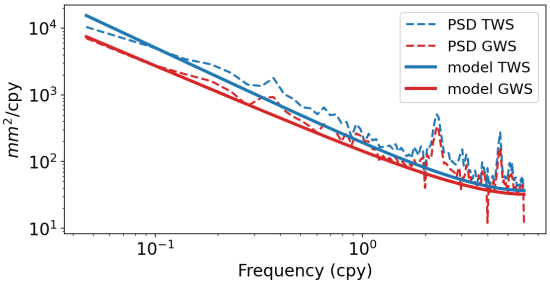

Figure 9: Globally averaged power spectral densities (PSDs) of TWS (blue) and GWS (red) residuals (dashed), together with the corresponding PLWN model fits (solid).

To post-fit validate the trend detection and water storage change quantification approach, we validate the use of power-law white noise (PLWN) models for both TWS and GWS by comparing empirical and modelled PSDs (Figure 9). The residual spectra show clear power-law behaviour, with reduced amplitudes across all frequencies following the G3P disaggregation. The PLWN fits reproduce the empirical PSDs well at low and intermediate frequencies (up to ∼1 cpy), which dominate long-term trend uncertainty. At higher frequencies, remaining intra-seasonal variability is not fully captured; however, this mismatch has negligible impact on trend uncertainty estimates, which are governed primarily by the low-frequency spectrum (e.g., Bos et al., 2020).

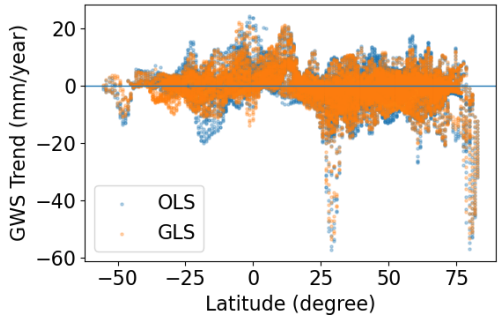

Figure 10: Latitudinal distribution of groundwater storage (GWS) trends estimated using ordinary least squares (OLS) and generalized least squares (GLS). Each point represents a grid-cell trend plotted as a function of latitude. Horizontal lines indicate zero trend.

3.4. Sensitivity of groundwater storage trends to regression method

A comparison between OLS and GLS trend estimates highlights the influence of noise modelling on derived GWS trends (Figure 10). When aggregated globally, area-weighted OLS trends yield a near-zero mean (-0.08 mm yr^{-1}) and a slightly positive median (0.22 mm yr^{-1}), whereas GLS estimates produce a more consistently negative signal, with a mean of -0.36 mm yr^{-1} and a median of -0.16 mm yr^{-1}. The latitudinal distribution further shows that GLS-derived trends show a reduced spread relative to OLS, which indicates better stability – this primarily reflects the down-weighting of interannual stochastic variability within the GLS framework. Overall, GLS trends are systematically shifted toward more negative values by approximately 0.3–0.4 mm yr^{-1} relative to OLS, while remaining small in magnitude at the global scale. All estimates shown here are derived from a 1° spatial

https://doi.org/10.5194/egusphere-2026-975
Preprint. Discussion started: 27 March 2026

grid following downsampling of the original data. This change in spatial resolution is not expected to materially affect the results, as spatial gradients in GWS trends are generally smooth between neighbouring grid cells.

4. Conclusion and Outlook

In this study we perform a consistent global assessment of statistically significant linear terrestrial (TWS) and groundwater storage (GWS) trends using the Global Gravity-based Groundwater Product (G3P) and 21.5 years of GRACE/GRACE-FO satellite gravimetry observations (2002–2023). Using a calibrated trend-analysis framework that accounts for seasonal and interannual variability as well as the memory properties of hydrological time series, we quantify continent-scale volumetric water storage changes from statistically significant trends and so separate persistent signals from stochastic (natural) variability and observation errors.

Our analysis confirms well-documented TWS patterns dominated by global-warming-induced ice and glacier mass loss, as well as groundwater depletion in intensively irrigated regions (e.g., Rodell et al., 2018; Scanlon et al., 2018), and reveals previously unresolved regional groundwater patterns. These include widespread and statistically significant GWS increases across large parts of Africa, newly detected groundwater declines in parts of Canada, Europe, and Russia indicative of emerging high-latitude drying, and spatially coherent GWS reductions in eastern Brazil and other drought-affected regions (e.g., South Africa, Madagascar).

At the global continental scale (excluding Greenland and Antarctica), we find significant net TWS losses of approximately -145 km^3 yr^{-1} and net GWS losses of -26.5 km^3 yr^{-1}. Total gross continental TWS losses amount to $\sim$194 km^3 yr^{-1}, of which gross groundwater loss – mostly by depletion - contributes $\sim$103 km^3 yr^{-1} ($\sim$53%). Glacier retreat remains the dominant contributor to the net TWS trend, and net groundwater losses represent only $\sim$18% of the continental net TWS balance due to substantial compensating recharge, particularly across Africa. Spectral analysis further demonstrates that GWS changes dominate the residual interannual TWS variability after removal of other storage compartments. Interannual variability in both TWS and GWS is well described by long-range dependent processes, whereas RZSM primarily governs seasonal variability and exhibits short-range memory.

Regionally, Asia exhibits the strongest groundwater declines (mostly from depletion, ~-55 km^3 yr^{-1}), driven by extraction in the Indo-Gangetic Plain, North China Plain, and the Middle East, where groundwater accounts for approximately 63% of the continental TWS decline and thus represents the dominant drying mechanism. In contrast, Africa shows widespread positive GWS trends ($\sim+37$ km^3 yr^{-1}), particularly across western, central, and eastern regions, which is consistent with sustained recharge linked to changing precipitation regimes. North America shows comparatively small net GWS losses concentrated in agricultural and drought-affected regions, with continental TWS decline largely governed by cryospheric losses in Alaska and Arctic regions. South America is dominated by strong seasonal variability and Patagonian glacier mass loss, so far limiting the detection of potentially-present groundwater trends. Across the Northern Hemisphere, larger areas of Canada and especially of Europe and Russia are tending towards negative groundwater trends, which reflects increasing climate-driven stress and broadly consistent with recent GRACE-based drying assessments (e.g., Chandanpurkar et al., 2025). Apparent negative GWS trends over parts of the Canadian Arctic Archipelago were excluded from continental budgets due to likely influences from leakage, GIA uncertainties, and potential compartment estimation limitations.

https://doi.org/10.5194/egusphere-2026-975
Preprint. Discussion started: 27 March 2026

Repeating the analysis at a 95% significance threshold confirms the robustness of these conclusions. Net continental TWS losses increase moderately from −145 to −161 km^3 yr^{-1}, and net GWS losses from −26.5 to −31.4 km^3 yr^{-1}. Gross continental TWS losses rise from 194 to 226 km^3 yr^{-1}, and gross groundwater depletion from 103 to 129 km^3 yr^{-1}. Importantly, the relative groundwater contribution changes only marginally (net: ∼18% to ∼20%; gross: ∼53% to ∼57%), which indicates on the robustness of the chosen trend analysis approach – the use of a strict 99% significance threshold shows that weak or noise-dominated trends may remain undetected. Importantly, the reduction from TWS to GWS not only isolates groundwater dynamics but also reduces interannual stochastic variability, leading to improved detectability of persistent groundwater change. Based on our analyses, we also find that global GRACE-derived TWS/GWS change estimates are sensitive to methodological choices. For example, Chandanpurkar et al. 2025 reported continental losses exceeding 300 km^3 yr^{-1} whereas our significance-constrained aggregation yields lower values, which are closer to aggregation of regionally-resolved analyses such as Rodell et al. 2018 and independent model-based groundwater depletion estimates (e.g., Döll et al., 2014). consequently, we expect our reported TWS and GWS volumetric change rates as conservative, reliable and robust bounds on global continental water storage change.

Regarding future work, an improved characterization of storage compartment components – particularly RZSM, SWS, and SWE, whose uncertainties directly affect GWS trend estimates in regions with weak signals or strong interannual variability – should be envisaged. Beside further compartment product analyses, an improved leakage treatment and refined GIA corrections are critical aspects for interpreting trends in high-latitude, glacier-dominated regions (such as the Canadian Arctic Archipelago). Cross-TWS-product evaluations have documented systematic differences between spherical-harmonic-based and mascon-based water storage products in drought recovery, hydrological memory, and precipitation–storage relationships across climate regimes (Akan et al., 2025), which raises the need for further analysis. Regions with GWS trends on the level to significance (e.g., in Europe, more general on the northern hemisphere) need continued monitoring, as persistent trends may intensify with longer observational records. Additional constraints from hydrological models, space-geodetic observations (e.g., GNSS, InSAR), and in-situ groundwater measurements will be essential for improved attribution of observed TWS and GWS changes. Extending the framework to longer time series, including upcoming GRACE-C and mass change missions, together with the integration of measurement stability uncertainty concepts (Gobron et al., 2026) (taking full leverage of validated G3P formal uncertainties), are expected to further enhance the reliablity of trend detection under the presented approach.

Data availability

The G3P v1.12 data used in this study are publicly available via the GFZ GravIS portal (https://gravis.gfz.de/gws).

The processed TWS and GWS time series and the resulting GLS parameter estimates are archived at Zenodo: https://doi.org/10.5281/zenodo.18538047.

Code availability

The Hector software (Bos et al., 2008, 2021), used for stochastic time-series modelling and variance component estimation, is publicly available at https://teromovigo.com/product/hector/ . All analyses were performed using this software together with standard scientific Python libraries. The complete statistical framework, including model equations and parameter estimation procedures, is described in Sect. 2.

https://doi.org/10.5194/egusphere-2026-975
Preprint. Discussion started: 27 March 2026

Author contributions

Roland Hohensinn (RH): Conceptualization; Methodology; Software; Formal analysis; Investigation; Data curation; Visualization; Writing – original draft; Writing – review & editing. Junyang Gou (JG): Conceptualization; Methodology; Software; Formal analysis; Investigation; Data curation; Visualization; Writing – review & editing. Ulrich Meyer (UM): Investigation; Data curation; Writing – original draft; Writing – review & editing. Vincent Humphrey (VH): Investigation; Writing – review & editing. Wouter Dorigo (WD): Investigation; Data curation; Writing – review & editing. Eva Boergens (EB): Investigation; Writing – review & editing. Benedikt Soja (BS): Investigation; Writing – review & editing. Alexander Gruber (AGr): Investigation; Writing – review & editing. Laura Jensen (LJ): Investigation; Writing – review & editing. Annette Eicker (AE): Investigation; Writing – review & editing. Michael Rast (MR): Investigation. Andreas Günther (AGü): Investigation; Data curation; Writing – original draft; Writing – review & editing.

Competing Interests

Co-author A. Gruber is member of the editorial board of the HESS journal. In addition to this, the authors declare that they have no competing interests.

Acknowledgments

A part of this study was performed during Roland Hohensinn's scientist visits at Scripps Institution of Oceanography, UCSD, and Junyang Gou's scientific visit at Bodner Lab, MIT.

References

Ahmed, M., Wiese, D.N., 2019. Short-term trends in Africa's freshwater resources: Rates and drivers. Science of the Total Environment 695, 133843.

Akan, A., Yılmaz, M.T., Dobslaw, H., Ince, E.S., Evrendilek, F., Förste, C., Yagci, A.L., 2025. Evaluation of globally gridded precipitation data and satellite-based terrestrial water storage products using hydrological drought recovery time. Hydrology and Earth System Sciences 29, 3359–3377. doi:10.5194/hess-29-3359-2025.

Albergel, C., De Rosnay, P., Gruhier, C., Muñoz-Sabater, J., Hasenauer, S., Isaksen, L., Kerr, Y., Wagner, W., 2012. Evaluation of remotely sensed and modelled soil moisture products using global ground-based in situ observations. Remote Sensing of Environment 118, 215–226.

Allen, M.R., Tett, S.F., 1999. Checking for model consistency in optimal fingerprinting. Climate Dynamics 15, 419–434.

Amiri-Simkooei, A., Hosseini-Asl, M., Asgari, J., Zangeneh-Nejad, F., 2019. Offset detection in GPS position time series using multivariate analysis. GPS solutions 23, 1–12.

Anyah, R., Forootan, E., Awange, J.L., Khaki, M., 2018. Understanding linkages between global climate indices and terrestrial water storage changes over Africa using GRACE products. Science of The Total Environment 635, 1405–1416.

Asoka, A., Gleeson, T., Wada, Y., Mishra, V., 2017. Relative contribution of monsoon precipitation and pumping to changes in groundwater storage in India. Nature Geoscience 10, 109–117. doi:10.1038/ngeo2869.

https://doi.org/10.5194/egusphere-2026-975
Preprint. Discussion started: 27 March 2026

966 Beltaos, S., Peters, D.L., 2024. Effects of regulation on open-water flows in the lower Peace
967 River, Canada, and implications for the recharge of Peace-Athabasca Delta basins. River
968 Research and Applications 40, 151–162.

969 Bhanja, S.N., Mukherjee, A., Rodell, M., Wada, Y., Chattopadhyay, S., Velicogna, I., Pan-
970 galuru, K., Famiglietti, J.S., 2017. Groundwater rejuvenation in parts of India influenced
971 by water-policy change implementation. Scientific reports 7, 7453.

972 Bierkens, M.F., Wada, Y., 2019. Non-renewable groundwater use and groundwater depletion:
973 a review. Environmental Research Letters 14, 063002. doi:10.1088/1748-9326/ab1a5f.

974 Bindoff, N.L., Stott, P.A., AchutaRao, K.M., Allen, M.R., Gillett, N., Gutzler, D., Hansingo,
975 K., Hegerl, G., Hu, Y., Jain, S., et al., 2014. Detection and attribution of climate change:
976 from global to regional. Climate change 2013: the physical science basis .

977 Boergens, E., Güntner, A., Sips, M., Schwatke, C., Dobslaw, H., 2024a. Interannual variations
978 of terrestrial water storage in the East African Rift region. Hydrology and Earth System
979 Sciences 28, 4733–4754. doi:10.5194/hess-28-4733-2024.

980 Boergens, E., Güntner, A., Sips, M., Schwatke, C., Dobslaw, H., 2024b. Interannual variations
981 of terrestrial water storage in the East African Rift region. EGUsphere 2024, 1–25.

982 Bonsal, B.R., Peters, D.L., Seglenieks, F., Rivera, A., Berg, A., 2019. Changes in freshwater
983 availability across Canada. Canada's changing climate report , 261–342.

984 Bos, M., Fernandes, R., Bastos, L., 2021. Hector user manual version 1.9. https://segal.
985 ubi.pt/wp-content/uploads/2021/05/hector_manual_1.9.pdf, last accessed 2024-01-
986 19,.

987 Bos, M., Fernandes, R., Williams, S., Bastos, L., 2008. Fast error analysis of continuous GPS
988 observations. Journal of Geodesy 82, 157–166.

989 Bos, M.S., Montillet, J.P., Williams, S.D., Fernandes, R.M., 2020. Introduction to geodetic
990 time series analysis, in: Geodetic Time Series Analysis in Earth Sciences. Springer, pp.
991 29–52.

992 Braun, M.H., Malz, P., Sommer, C., Farías-Barahona, D., Sauter, T., Casassa, G., Soruco,
993 A., Skvarca, P., Seehaus, T.C., 2019. Constraining glacier elevation and mass changes
994 in South America. Nature Climate Change 9, 130–136. doi:https://doi.org/10.1038/
995 s41558-018-0375-7.

996 Bring, A., Fedorova, I., Dibike, Y., Hinzman, L., Mård, J., Mernild, S.H., Prowse, T., Se-
997 menova, O., Stuefer, S.L., Woo, M.K., 2016. Arctic terrestrial hydrology: A synthesis
998 of processes, regional effects, and research challenges. Journal of Geophysical Research:
999 Biogeosciences 121, 621–649. doi:10.1002/2015JG003131.

1000 Bulygina, O.N., Groisman, P.Y., Razuvaev, V.N., Korshunova, N.N., 2011. Changes in snow
1001 cover characteristics over Northern Eurasia since 1966. Environmental Research Letters 6,
1002 045204. doi:10.1088/1748-9326/6/4/045204.

1003 Cao, G., Zheng, C., Scanlon, B.R., Liu, J., Li, W., 2013. Use of flow modeling to assess sus-
1004 tainability of groundwater resources in the North China Plain. Water Resources Research
1005 49, 159–175. doi:https://doi.org/10.1029/2012WR011899.

https://doi.org/10.5194/egusphere-2026-975
Preprint. Discussion started: 27 March 2026

Chandanpurkar, H.A., Famiglietti, J.S., Gopalan, K., Wiese, D.N., Wada, Y., Kakinuma, K., Reager, J.T., Zhang, F., 2025. Unprecedented continental drying, shrinking freshwater availability, and increasing land contributions to sea level rise. Science Advances 11, eadx0298.

Chandanpurkar, H.A., Fasullo, J.T., Reager, J.T., Hamlington, B.D., 2021. A note on spectral representation of cyclostationary GRACE-TWS signals. Geophysical Research Letters 48, e2021GL093278. doi:10.1029/2021GL093278.

Chaudhari, S., Pokhrel, Y., Moran, E., Miguez-Macho, G., 2019. Multi-decadal hydrologic change and variability in the Amazon River basin: understanding terrestrial water storage variations and drought characteristics. Hydrology and Earth System Sciences 23, 2841–2862.

Chen, J., Pekker, T., Wilson, C.R., Tapley, B.D., Kostianoy, A., Cretaux, J.F., Safarov, E., 2017. Long-term Caspian sea level change. Geophysical Research Letters 44, 6993–7001.

Chen, J., Wilson, C., Tapley, B., 2006. Satellite gravity measurements confirm accelerated melting of Greenland ice sheet. science 313, 1958–1960. doi:https://doi.org/10.1126/science.1129007.

Chen, J., Wilson, C., Tapley, B., Longuevergne, L., Yang, Z., Scanlon, B., 2010. Recent La Plata basin drought conditions observed by satellite gravimetry. Journal of Geophysical Research: Atmospheres 115.

Cheon, S.H., Hamlington, B.D., Reager, J.T., Chandanpurkar, H.A., 2021. Identifying ENSO-related interannual and decadal variability on terrestrial water storage. Scientific Reports 11, 13595. doi:10.1038/s41598-021-92729-4.

Choulga, M., Moschini, F., Mazzetti, C., Grimaldi, S., Disperati, J., Beck, H., Salamon, P., Prudhomme, C., 2024. Technical note: Surface fields for global environmental modelling. Hydrology and Earth System Sciences 28, 2991–3036. doi:10.5194/hess-28-2991-2024.

Ciracì, E., Velicogna, I., Swenson, S., 2020. Continuity of the mass loss of the world's glaciers and ice caps from the GRACE and GRACE follow-on missions. Geophysical Research Letters 47, e2019GL086926.

Cook, B.I., Mankin, J.S., Marvel, K., Williams, A.P., Smerdon, J.E., Anchukaitis, K.J., 2020. Twenty-first century drought projections in the CMIP6 forcing scenarios. Earth's Future 8, e2019EF001461. doi:10.1029/2019EF001461.

Cui, L., Zhu, C., Wu, Y., Yao, C., Wang, X., An, J., Wei, P., 2022. Natural-and human-induced influences on terrestrial water storage change in Sichuan, Southwest China from 2003 to 2020. Remote Sensing 14, 1369.

Dahle, C., Boergens, E., Sasgen, I., Döhne, T., Reißland, S., Dobslaw, H., Klemann, V., Murböck, M., König, R., Dill, R., Sips, M., Sylla, U., Groh, A., Horwath, M., Flechtner, F., 2025. GravIS: Mass anomaly products from satellite gravimetry. Earth System Science Data 17, 611–631. doi:10.5194/essd-17-611-2025.

Dangar, S., Asoka, A., Mishra, V., 2021. Causes and implications of groundwater depletion in India: A review. Journal of Hydrology 596, 126103. doi:https://doi.org/10.1016/j.jhydrol.2021.126103.

https://doi.org/10.5194/egusphere-2026-975
Preprint. Discussion started: 27 March 2026

Döll, P., Müller Schmied, H., Schuh, C., Portmann, F.T., Eicker, A., 2014. Global-scale assessment of groundwater depletion and related groundwater abstractions: Combining hydrological modeling with information from well observations and GRACE satellites. Water Resources Research 50, 5698–5720. doi:10.1002/2014WR015595.

Dorigo, W., Dietrich, S., Aires, F., Brocca, L., Carter, S., Cretaux, J.F., Dunkerley, D., Enomoto, H., Forsberg, R., Güntner, A., et al., 2021. Closing the water cycle from observations across scales: Where do we stand? Bulletin of the American Meteorological Society 102, E1897–E1935.

Dubois, E., Larocque, M., Gagné, S., Braun, M., 2022. Climate change impacts on groundwater recharge in cold and humid climates: Controlling processes and thresholds. Climate 10, 6.

Dussaillant, I., Bannwart, J., Paul, F., Zemp, M., 2023. Glacier mass change global gridded data from 1976 to present derived from the fluctuations of glaciers database. world glacier monitoring service. doi:10.24381/cds.ba597449.

Eicker, A., Schawohl, L., Middendorf, K., Bagge, M., Jensen, L., Dobslaw, H., 2024. Influence of GIA uncertainty on climate model evaluation with GRACE/GRACE-FO satellite gravimetry data. Journal of Geophysical Research: Solid Earth 129, e2023JB027769.

Famiglietti, J.S., Lo, M., Ho, S.L., Bethune, J., Anderson, K., Syed, T.H., Swenson, S.C., de Linage, C.R., Rodell, M., 2011. Satellites measure recent rates of groundwater depletion in California's Central Valley. Geophysical Research Letters 38. doi:https://doi.org/10.1029/2010GL046442.

Fatolazadeh, F., Goïta, K., 2021. Mapping terrestrial water storage changes in Canada using GRACE and GRACE-FO. Science of The Total Environment 779, 146435. doi:10.1016/j.scitotenv.2021.146435.

Favreau, G., Cappelaere, B., Massuel, S., Leblanc, M., Boucher, M., Boulain, N., Leduc, C., 2009. Land clearing, climate variability, and water resources increase in semiarid southwest Niger: A review. Water Resources Research 45.

Felfelani, F., Wada, Y., Longuevergne, L., Pokhrel, Y.N., 2017. Natural and human-induced terrestrial water storage change: A global analysis using hydrological models and GRACE. Journal of Hydrology 553, 105–118.

Feng, W., Zhong, M., Lemoine, J.M., Biancale, R., Hsu, H.T., Xia, J., 2013a. Evaluation of groundwater depletion in North China using the Gravity Recovery and Climate Experiment (GRACE) data and ground-based measurements. Water Resources Research 49, 2110–2118. doi:https://doi.org/10.1002/wrcr.20192.

Feng, W., Zhong, M., Lemoine, J.M., Biancale, R., Hsu, H.T., Xia, J., 2013b. Evaluation of groundwater depletion in North China using the Gravity Recovery and Climate Experiment (GRACE) data and ground-based measurements. Water Resources Research 49, 2110–2118. doi:10.1002/wrcr.20192.

Franzke, C., 2012. Nonlinear trends, long-range dependence, and climate noise properties of surface temperature. Journal of Climate 25, 4172–4183.

Franzke, C.L., O'Kane, T.J., 2017. Nonlinear and stochastic climate dynamics. Cambridge University Press.

https://doi.org/10.5194/egusphere-2026-975
Preprint. Discussion started: 27 March 2026

Frappart, F., 2020. Groundwater storage changes in the major north african transboundary aquifer systems during the GRACE era (2003–2016). Water 12, 2669.

Frappart, F., Ramillien, G., 2018. Monitoring groundwater storage changes using the gravity recovery and climate experiment (GRACE) satellite mission: A review. Remote Sensing 10. doi:10.3390/rs10060829.

Frederikse, T., Landerer, F., Caron, L., Adhikari, S., Parkes, D., Humphrey, V.W., Dangendorf, S., Hogarth, P., Zanna, L., Cheng, L., et al., 2020. The causes of sea-level rise since 1900. Nature 584, 393–397. doi:https://doi.org/10.1038/s41586-020-2591-3.

Gbetkom, P.G., Crétaux, J.F., Biancamaria, S., Blazquez, A., Paris, A., Tchilibou, M., Gal, L., Kitambo, B., Oliveira, R.A.J., Gosset, M., 2024. Lake Tanganyika basin water storage variations from 2003–2021 for water balance and flood monitoring. Remote Sensing Applications: Society and Environment 34, 101182.

Gobron, K., Hohensinn, R., Loizeau, X., Bulgin, C.E., Merchant, C.J., Woolliams, E.R., Cox, M.G., Dorigo, W., Howard, T., Langsdale, M., et al., 2026. A unified framework for trend uncertainty assessment in climate data records: Demonstration on global mean sea level. Surveys in Geophysics , 1–34.

Gobron, K., Rebischung, P., de Viron, O., Demoulin, A., Van Camp, M., 2022. Impact of offsets on assessing the low-frequency stochastic properties of geodetic time series. Journal of Geodesy 96, 46.

Goncalves, J., Petersen, J., Deschamps, P., Hamelin, B., Baba-Sy, O., 2013. Quantifying the modern recharge of the "fossil" Sahara aquifers. Geophysical Research Letters 40, 2673–2678.

Gong, H., Pan, Y., Zheng, L., Li, X., Zhu, L., Zhang, C., Huang, Z., Li, Z., Wang, H., Zhou, C., 2018. Long-term groundwater storage changes and land subsidence development in the North China Plain (1971–2015). Hydrogeology Journal 26, 1417–1427.

Gonzales, L., López, V., Huamán, D., Villalobos, C., Espinoza, R., Vega, M., Ramos, J., 2025. Two decades of groundwater variability in Peru using satellite gravimetry data. Applied Sciences 15, 8071. doi:10.3390/app15148071. published 20 July 2025.

Gou, J., Börger, L., Schindelegger, M., Soja, B., 2025. Downscaling GRACE-derived ocean bottom pressure anomalies using self-supervised data fusion. Journal of Geodesy 99, 19. doi:https://doi.org/10.1007/s00190-025-01943-9.

Gou, J., Soja, B., 2024. Global high-resolution total water storage anomalies from self-supervised data assimilation using deep learning algorithms. Nature Water 2, 139–150. doi:10.1038/s44221-024-00194-w.

de Graaf, I.E., van Beek, R.L., Gleeson, T., Moosdorf, N., Schmitz, O., Sutanudjaja, E.H., Bierkens, M.F., 2017. A global-scale two-layer transient groundwater model: Development and application to groundwater depletion. Advances in water Resources 102, 53–67.

Gronewold, A.D., Rood, R.B., 2019. Recent water level changes across Earth's largest lake system and implications for future variability. Journal of Great Lakes Research 45, 1–3. doi:https://doi.org/10.1016/j.jglr.2018.10.012.

https://doi.org/10.5194/egusphere-2026-975
Preprint. Discussion started: 27 March 2026

Gunes, O., Aydin, C., 2024. Colored noise in GRACE total water storage time series: Its impact on trend significance in the Türkiye region and major world river basins. Advances in Space Research 74, 1633–1647. doi:https://doi.org/10.1016/j.asr.2024.05.051.

Güntner, A., Sharifi, E., Haas, J., Boergens, E., Cao, F., Dahle, C., Darbeheshti, N., Dobslaw, H., Dussaillant, I., Dorigo, W., et al., 2026. The global gravity-based groundwater product (G3P). Earth System Science Data Discussions 2026, 1–48.

Güntner, A., Sharifi, E., Haas, J., Boergens, E., Dahle, C., Dobslaw, H., Dorigo, W., Dussailant, I., Flechtner, F., Jäggi, A., Kosmale, M., Luojus, K., Mayer-Gürr, T., Meyer, U., Preimesberger, W., Ruz Vargas, C., Zemp, M., 2024. Global Gravity-based Groundwater Product (G3P) V.1.12. GFZ Data Services doi:10.5880/g3p.2024.001.

Haacker, E.M., Kendall, A.D., Hyndman, D.W., 2016. Water level declines in the High Plains Aquifer: Predevelopment to resource senescence. Groundwater 54, 231–242. doi:https://doi.org/10.1111/gwat.12350.

Hamdi, M., Goïta, K., 2023. Analysis of groundwater depletion in the saskatchewan river basin in Canada from coupled SWAT-MODFLOW and satellite gravimetry. Hydrology 10, 188.

Hamlington, B.D., Reager, J.T., Chandanpurkar, H.A., Kim, K.Y., 2019. Amplitude modulation of seasonal variability in terrestrial water storage. Geophysical Research Letters 46, 4404–4412. doi:10.1029/2019GL082272.

Hasselmann, K., 1997. Multi-pattern fingerprint method for detection and attribution of climate change. Climate dynamics 13, 601–611.

Hernández, A., García-Sanz, I., Heine-Fuster, I., Luque, J.A., Aránguiz-Acuña, A., Parra, P., Pedreros-Guarda, P., Pérez-Martínez, C., 2021. Limnological response from high-altitude wetlands to the water supply in the Andean Altiplano. Scientific Reports 11, 7681. doi:10.1038/s41598-021-87162-6.

Hirschi, M., Stradiotti, P., Crezee, B., Dorigo, W., Seneviratne, S.I., 2025. Potential of long-term satellite observations and reanalysis products for characterising soil drying: trends and drought events. Hydrology and Earth System Sciences 29, 397–425.

Hoell, A., Gaughan, A.E., Shukla, S., Magadzire, T., 2017. The hydrologic effects of synchronous El Niño–Southern oscillation and subtropical Indian ocean dipole events over Southern Africa. Journal of Hydrometeorology 18, 2407–2424.

Hohensinn, R., Ruttner, P., Bock, Y., 2024. Sensitivity of GNSS to vertical land motion over Europe: effects of geophysical loadings and common-mode errors. Journal of Geodesy 98, 68.

Huang, J., Halpenny, J., Van Der Wal, W., Klatt, C., James, T., Rivera, A., 2012. Detectability of groundwater storage change within the great lakes water basin using GRACE. Journal of Geophysical Research: Solid Earth 117.

Huang, Q., Wang, P., Wang, R., Yu, J., Frolova, N.L., Pozdniakov, S.P., 2025. Differential decline in terrestrial water storage across major permafrost-dominated Arctic River basins during the rapid warming period from 1981 to 2020. Journal of Geophysical Research: Atmospheres 130, e2024JD042978.

https://doi.org/10.5194/egusphere-2026-975
Preprint. Discussion started: 27 March 2026

Huggins, X., Gleeson, T., Kummu, M., Zipper, S.C., Wada, Y., Troy, T.J., Famiglietti, J.S., 2022. Hotspots for social and ecological impacts from freshwater stress and storage loss. Nature Communications 13, 439.

Humphrey, V., Gudmundsson, L., 2019. GRACE-REC: a reconstruction of climate-driven water storage changes over the last century. Earth System Science Data 11, 1153–1170. doi:https://doi.org/10.5194/essd-11-1153-2019.

Humphrey, V., Gudmundsson, L., Seneviratne, S.I., 2016. Assessing global water storage variability from GRACE: Trends, seasonal cycle, subseasonal anomalies and extremes. Surveys in geophysics 37, 357–395. doi:https://doi.org/10.1007/s10712-016-9367-1.

Humphrey, V., Gudmundsson, L., Seneviratne, S.I., 2017. A global reconstruction of climate-driven subdecadal water storage variability. Geophysical Research Letters 44, 2300–2309. doi:10.1002/2017GL072564.

Humphrey, V., Rodell, M., Eicker, A., 2023. Using satellite-based terrestrial water storage data: a review. Surveys in Geophysics 44, 1489–1517.

Jackson, C.R., Bloomfield, J.P., Mackay, J.D., 2015. Evidence for changes in historic and future groundwater levels in the UK. Progress in Physical Geography 39, 49–67.

Jacob, T., Wahr, J., Pfeffer, W.T., Swenson, S., 2012. Recent contributions of glaciers and ice caps to sea level rise. Nature 482, 514–518.

Jäggi, A., Meyer, U., Lasser, M., Jenny, B., Lopez, T., Flechtner, F., Dahle, Christophand Förste, C., Mayer-Gürr, T., Kvas, A., Lemoine, J.M., Bourgogne, S., Weigelt, M., Groh, A., 2020. International combination service for time-variable gravity fields (COST-G) - start of operational phase and future perspectives. International Association of Geodesy Symposia 152, 57–65. doi:10.1007/1345_2020_109.

Jarugula, S., McPhaden, M.J., 2023. Indian ocean dipole affects eastern tropical Atlantic salinity through Congo River Basin hydrology. Communications Earth & Environment 4, 366.

Jasechko, S., Seybold, H., Perrone, D., Fan, Y., Shamsudduha, M., Taylor, R.G., Fallatah, O., Kirchner, J.W., 2024. Rapid groundwater decline and some cases of recovery in aquifers globally. Nature 625, 715–721.

Jensen, L., Eicker, A., Dobslaw, H., Pail, R., 2020. Emerging changes in terrestrial water storage variability as a target for future satellite gravity missions. Remote Sensing 12, 3898. doi:10.3390/rs12233898.

Jensen, L., Eicker, A., Dobslaw, H., Stacke, T., Humphrey, V., 2019. Long-term wetting and drying trends in land water storage derived from GRACE and CMIP5 models. Journal of Geophysical Research: Atmospheres 124, 9808–9823.

Jiang, Y., Zhou, L., Roundy, P.E., Hua, W., Raghavendra, A., 2021. Increasing influence of Indian Ocean dipole on precipitation over central equatorial Africa. Geophysical Research Letters 48, e2020GL092370.

Joodaki, G., Wahr, J., Swenson, S., 2014. Estimating the human contribution to groundwater depletion in the Middle East, from GRACE data, land surface models, and well observations. Water Resources Research 50, 2679–2692.

https://doi.org/10.5194/egusphere-2026-975
Preprint. Discussion started: 27 March 2026

Kayastha, M.B., Ye, X., Huang, C., Xue, P., 2022. Future rise of the Great Lakes water levels under climate change. Journal of Hydrology 612, 128205. doi:10.1016/j.jhydrol.2022.128205.

Kirshen, A.B., Moran, B.J., Munk, L.A., Russo, A.A., McKnight, S.V., Jenckes, J., Corkran, D.B., Bresee, M., Boutt, D.F., 2025. Freshwater inflows to closed basins of the Andean plateau in Chile, Argentina, and Bolivia. Communications Earth & Environment 6, 177.

Klos, A., Hunegnaw, A., Teferle, F.N., Abraha, K.E., Ahmed, F., Bogusz, J., 2018. Statistical significance of trends in zenith wet delay from re-processed GPS solutions. GPS Solutions 22, 51.

Knief, U., Forstmeier, W., 2021. Violating the normality assumption may be the lesser of two evils. Behavior Research Methods 53, 2576–2590.

Konikow, L.F., 2015. Long-term groundwater depletion in the United States. Groundwater 53, 2–9. doi:https://doi.org/10.1111/gwat.12306.

Koscielny-Bunde, E., Kantelhardt, J.W., Braun, P., Bunde, A., Havlin, S., 2006. Long-term persistence and multifractality of river runoff records: Detrended fluctuation studies. Journal of Hydrology 322, 120–137. doi:10.1016/j.jhydrol.2005.03.004.

Koutsoyiannis, D., 2003. Climate change, the hurst phenomenon, and hydrological statistics. Hydrological Sciences Journal 48, 3–24.

Kvas, A., Boergens, E., Dobslaw, H., Eicker, A., Mayer-Guerr, T., Güntner, A., 2024. Evaluating long-term water storage trends in small catchments and aquifers from a joint inversion of 20 years of GRACE/GRACE-FO mission data. Geophysical Journal International 236, 1002–1012.

Lai, E.N., Wang-Erlandsson, L., Virkki, V., Porkka, M., Van Der Ent, R.J., 2023. Root zone soil moisture in over 25% of global land permanently beyond pre-industrial variability as early as 2050 without climate policy. Hydrology and Earth System Sciences 27, 3999–4018.

Landerer, F.W., Flechtner, F.M., Save, H., Webb, F.H., Bandikova, T., Bertiger, W.I., Bettadpur, S.V., Byun, S.H., Dahle, C., Dobslaw, H., et al., 2020. Extending the global mass change data record: GRACE follow-on instrument and science data performance. Geophysical Research Letters 47, e2020GL088306.

Leduc, C., Favreau, G., Schroeter, P., 2001. Long-term rise in a Sahelian water-table: The continental terminal in south-west Niger. Journal of hydrology 243, 43–54.

Li, B., Rodell, M., 2024. Terrestrial water storage in 2023. Nature Reviews Earth & Environment 5, 247–249.

Li, J., Wang, S., 2022. Seasonal variations and long-term trends of groundwater over the Canadian landmass. Hydrogeology Journal 30, 401–415. doi:10.1007/s10040-022-02460-1.

Li, J., Wang, S., Zhou, F., 2016. Time series analysis of long-term terrestrial water storage over Canada from GRACE satellites using principal component analysis. Canadian Journal of Remote Sensing 42, 161–170. doi:10.1080/07038992.2016.1166042.

https://doi.org/10.5194/egusphere-2026-975
Preprint. Discussion started: 27 March 2026

Li, Z., Zhang, Y.K., 2007. Quantifying fractal dynamics of groundwater systems with detrended fluctuation analysis. Journal of hydrology 336, 139–146.

Lin, H., Cheng, X., Zheng, L., Peng, X., Feng, W., Peng, F., 2022. Recent changes in groundwater and surface water in large pan-arctic river basins. Remote Sensing 14, 607.

Little, M.A., Bloomfield, J.P., 2010. Robust evidence for random fractal scaling of groundwater levels in unconfined aquifers. Journal of hydrology 393, 362–369.

Lu, J., Kong, D., Zhang, Y., Xie, Y., Gu, X., Gulakhmadov, A., 2025. Hotspots of global water resource changes and their causes. Earth's Future 13, e2024EF005461. doi:https://doi.org/10.1029/2024EF005461.

Lucas, M.C., Kublik, N., Rodrigues, D.B.B., Meira Neto, A.A., Almagro, A., de Melo, D.C.D., Zipper, S.C., de Oliveira, P.T.S., 2021. Significant baseflow reduction in the São Francisco River Basin. Water 13. doi:10.3390/w13010002. published 22 December 2020.

Luojus, K., Pulliainen, J., Takala, M., Lemmetyinen, J., Mortimer, C., Derksen, C., Mudryk, L., Moisander, M., Hiltunen, M., Smolander, T., Ikonen, J., Cohen, J., Salminen, M., Norberg, J., Veijola, K., Venäläinen, P., 2021. GlobSnow v3.0 northern hemisphere snow water equivalent dataset. Scientific Data 8. doi:10.1038/s41597-021-00939-2.

MacDonald, A.M., Bonsor, H.C., Dochartaigh, B.É.Ó., Taylor, R.G., 2012. Quantitative maps of groundwater resources in Africa. Environmental Research Letters 7, 024009. doi:https://doi.org/10.1088/1748-9326/7/2/024009.

MacQueen, J., 1967. Some methods for classification and analysis of multivariate observations, in: Proceedings of the Fifth Berkeley Symposium on Mathematical Statistics and Probability, Volume 1: Statistics, University of California press. pp. 281–298.

Mandelbrot, B.B., Wallis, J.R., 1969. Some long-run properties of geophysical records. Water resources research 5, 321–340.

de Melo, D.C.D., Wendland, E., 2020. Using GRACE to quantify the depletion of terrestrial water storage in northeastern Brazil: The Urucuia aquifer system. Science of The Total Environment 705, 135828. doi:10.1016/j.scitotenv.2019.135828.

Merchant, C.J., Paul, F., Popp, T., Ablain, M., Bontemps, S., Defourny, P., Hollmann, R., Lavergne, T., Laeng, A., De Leeuw, G., et al., 2017. Uncertainty information in climate data records from Earth observation. Earth System Science Data 9, 511–527.

Meyer, U., Lasser, M., Dahle, C., Förste, C., Behzadpour, S., Koch, Jäggi, A., 2023. Combined monthly GRACE-FO gravity fields for a global gravity-based groundwater product. Geophysical Journal International 236, 456–469. doi:10.1093/gji/ggad437.

Micklin, P., 2016. The future Aral Sea: hope and despair. Journal of Environmental Geography 9, 1–15. doi:10.1515/jengeo-2016-0001.

Moihamette, F., Pokam, W.M., Diallo, I., Washington, R., 2024. Response of regional circulation features to the Indian Ocean dipole and influence on Central Africa climate. Climate Dynamics 62, 1–21.

Montillet, J.P., Bos, M.S., 2019. Geodetic time series analysis in earth sciences. Springer.

https://doi.org/10.5194/egusphere-2026-975
Preprint. Discussion started: 27 March 2026

Mudelsee, M., 2010. Climate Time Series Analysis: Classical Statistical and Bootstrap Methods. Springer, Dordrecht, Netherlands. doi:10.1007/978-90-481-9482-7.

Mudelsee, M., 2019. Trend analysis of climate time series: A review of methods. Earth-Science Reviews 190, 310–322. URL: https://www.sciencedirect.com/science/article/pii/S0012825218303726, doi:https://doi.org/10.1016/j.earscirev.2018.12.005.

Muskett, R.R., Romanovsky, V.E., 2011. Alaskan permafrost groundwater storage changes derived from GRACE and ground measurements. Remote Sensing 3, 378–397. doi:10.3390/rs3020378.

Naumann, G., Cammalleri, C., Mentaschi, L., Vogt, J., 2022. Extreme and Long-Term Drought in the La Plata Basin: Event Evolution and Impact Assessment until September 2022. Technical Report JRC132245. Joint Research Centre (JRC), European Commission. Luxembourg. URL: https://publications.jrc.ec.europa.eu/repository/handle/JRC132245.

Ni, S., Chen, J., Wilson, C.R., Li, J., Hu, X., Fu, R., 2018. Global terrestrial water storage changes and connections to ENSO events. Surveys in Geophysics 39, 1–22.

Nikraftar, Z., Parizi, E., Saber, M., Hosseini, S.M., Ataie-Ashtiani, B., Simmons, C.T., 2024. Groundwater sustainability assessment in the Middle East using GRACE/GRACE-FO data. Hydrogeology Journal 32, 321–337.

Orth, R., Seneviratne, S.I., 2012. Analysis of soil moisture memory from observations in europe. Journal of Geophysical Research: Atmospheres 117, D15115. doi:10.1029/2011JD017366.

Orth, R., Staudinger, M., Seneviratne, S.I., 2013. Inferring soil moisture memory from streamflow observations using a simple water balance model. Journal of Hydrometeorology 14, 1773–1790. doi:10.1175/JHM-D-12-099.1.

Otosaka, I.N., Shepherd, A., Ivins, E.R., Schlegel, N.J., Amory, C., van den Broeke, M., Horwath, M., Joughin, I., King, M., Krinner, G., et al., 2022. Mass balance of the Greenland and Antarctic ice sheets from 1992 to 2020. Earth System Science Data Discussions 2022, 1–33.

Pasik, A., Gruber, A., Preimesberger, W., De Santis, D., Dorigo, W., 2023. Uncertainty estimation for a new exponential-filter-based long-term root-zone soil moisture dataset from Copernicus Climate Change Service (C3S) surface observations. Geoscientific Model Development 16, 4957–4976. doi:10.5194/gmd-16-4957-2023.

Patterson, H.D., Thompson, R., 1971. Recovery of inter-block information when block sizes are unequal. Biometrika 58, 545–554.

Pfeffer, J., Cazenave, A., Barnoud, A., 2022. Analysis of the interannual variability in satellite gravity solutions: detection of climate modes fingerprints in water mass displacements across continents and oceans. Climate Dynamics 58, 1065–1084.

Piao, S., Wang, X., Park, T., Chen, C., Lian, X., He, Y., Bjerke, J.W., Chen, A., Ciais, P., Tømmervik, H., Nemani, R.R., Myneni, R.B., 2020. Characteristics, drivers and feedbacks of global greening. Nature Reviews Earth & Environment 1, 14–27. doi:10.1038/s43017-019-0001-x.

https://doi.org/10.5194/egusphere-2026-975
Preprint. Discussion started: 27 March 2026

Pokhrel, Y., Felfelani, F., Satoh, Y., Boulange, J., Burek, P., Gädeke, A., Gerten, D., Gosling, S.N., Grillakis, M., Gudmundsson, L., et al., 2021. Global terrestrial water storage and drought severity under climate change. Nature Climate Change 11, 226–233. doi:https://doi.org/10.1038/s41558-020-00972-w.

Preimesberger, W., Stradiotti, P., Dorigo, W., 2025. ESA CCI soil moisture gapfilled: an independent global gap-free satellite climate data record with uncertainty estimates. Earth System Science Data 17, 4305–4329.

Richey, A.S., Thomas, B.F., Lo, M.H., Reager, J.T., Famiglietti, J.S., Voss, K., Swenson, S., Rodell, M., 2015. Quantifying renewable groundwater stress with GRACE. Water Resources Research 51, 5217–5238. doi:10.1002/2015WR017349.

Riva, R.E., Bamber, J.L., Lavallée, D.A., Wouters, B., 2010. Sea-level fingerprint of continental water and ice mass change from GRACE. Geophysical Research Letters 37. doi:https://doi.org/10.1029/2010GL044770.

Rodell, M., Famiglietti, J.S., Wiese, D.N., Reager, J., Beaudoing, H.K., Landerer, F.W., Lo, M.H., 2018. Emerging trends in global freshwater availability. Nature 557, 651–659.

Rodell, M., Velicogna, I., Famiglietti, J.S., 2009. Satellite-based estimates of groundwater depletion in India. Nature 460, 999–1002. doi:https://doi.org/10.1038/nature08238.

Roe, G.H., 2011. What do glaciers tell us about climate variability and climate change? Journal of Glaciology 57, 567–578. doi:10.3189/002214311796905640.

Saito, Y.K., Justino, F., Gurjão, C.D., Zita, L., Paixão, P., Ramiro, Í., 2025. Soil moisture dynamics in South America: A multi-dataset analysis from 1990 to 2020. International Journal of Climatology , e70047.

Satizábal-Alarcón, D.A., Suhogusoff, A., Ferrari, L.C., 2024. Characterization of groundwater storage changes in the Amazon river basin based on downscaling of GRACE/GRACE-FO data with machine learning models. Science of The Total Environment 912, 168958.

Scanlon, B.R., Faunt, C.C., Longuevergne, L., Reedy, R.C., Alley, W.M., McGuire, V.L., McMahon, P.B., 2012. Groundwater depletion and sustainability of irrigation in the US High Plains and Central Valley. Proceedings of the national academy of sciences 109, 9320–9325. doi:https://doi.org/10.1073/pnas.1200311109.

Scanlon, B.R., Zhang, Z., Save, H., Sun, A.Y., Müller Schmied, H., Van Beek, L.P., Wiese, D.N., Wada, Y., Long, D., Reedy, R.C., et al., 2018. Global models underestimate large decadal declining and rising water storage trends relative to GRACE satellite data. Proceedings of the National Academy of Sciences 115, E1080–E1089. doi:https://doi.org/10.1073/pnas.1704665115.

Scanlon, B.R., Zhang, Z., Save, H., Wiese, D.N., Landerer, F.W., Long, D., Longuevergne, L., Chen, J., 2016. Global evaluation of new GRACE mascon products for hydrologic applications. Water Resources Research 52, 9412–9429. doi:https://doi.org/10.1002/2016WR019494.

Schilling, J., Hertig, E., Tramblay, Y., Scheffran, J., 2020. Climate change vulnerability, water resources and social implications in North Africa. Regional Environmental Change 20, 15.

https://doi.org/10.5194/egusphere-2026-975
Preprint. Discussion started: 27 March 2026

Seo, K.W., Ryu, D., Jeon, T., Youm, K., Kim, J.S., Oh, E.H., Chen, J., Famiglietti, J.S., Wilson, C.R., 2025. Abrupt sea level rise and Earth's gradual pole shift reveal permanent hydrological regime changes in the 21st century. Science 387, 1408–1413. doi:https://doi.org/10.1126/science.adq6529.

Shahgedanova, M., Afzal, M., Hagg, W., Kapitsa, V., Kasatkin, N., Mayr, E., Rybak, O., Saidaliyeva, Z., Severskiy, I., Usmanova, Z., Wade, A., Yaitskaya, N., Zhumabayev, D., 2020. Emptying water towers? Impacts of future climate and glacier change on river discharge in the Northern Tien Shan, Central Asia. Water 12, 627. doi:10.3390/w12030627.

Shalby, A., Emara, S.R., Metwally, M.I., Armanuos, A.M., El-Agha, D.E., Negm, A.M., Gado, T.A., 2023. Satellite-based estimates of groundwater storage depletion over Egypt. Environmental Monitoring and Assessment 195, 594.

Sharifi, E., Haas, J., Boergens, E., Dobslaw, H., Güntner, A., 2025. GRACE-compatible filtering of water storage data sets via spatial autocorrelation analysis. Hydrology and Earth System Sciences 29, 6985–6998.

Shrestha, R.R., Dibike, Y.B., Prowse, T.D., 2012. Modelling of climate-induced hydrologic changes in the lake winnipeg watershed. Journal of Great Lakes Research 38, 83–94.

Singh, A., Seitz, F., Schwatke, C., 2012. Inter-annual water storage changes in the Aral Sea from multi-mission satellite altimetry, optical remote sensing, and GRACE satellite gravimetry. Remote Sensing of Environment 123, 187–195. doi:10.1016/j.rse.2012.01.001.

Sospedra-Alfonso, R., Merryfield, W.J., Kharin, V.V., 2016. Representation of snow in the Canadian seasonal to interannual prediction system. part ii: Potential predictability and hindcast skill. Journal of Hydrometeorology 17, 2511–2535. doi:10.1175/JHM-D-16-0027.1.

Spinoni, J., Naumann, G., Carrao, H., Barbosa, P., Vogt, J., et al., 2014. World drought frequency, duration, and severity for 1951–2010. Int. J. Climatol 34, 2792–2804.

Spinoni, J., Naumann, G., Vogt, J., Barbosa, P., 2016. Meteorological droughts in Europe: events and impacts-past trends and future projections. Publications Office of the European Union.

Springer, A., Lopez, T., Owor, M., Frappart, F., Stieglitz, T., 2023. The role of space-based observations for groundwater resource monitoring over Africa. Surveys in Geophysics 44, 123–172. doi:https://doi.org/10.1007/s10712-022-09759-4.

Steffen, H., Petrovic, S., Müller, J., Schmidt, R., Wünsch, J., Barthelmes, F., Kusche, J., 2009. Significance of secular trends of mass variations determined from GRACE solutions. Journal of Geodynamics 48, 157–165. URL: https://www.sciencedirect.com/science/article/pii/S0264370709000969, doi:https://doi.org/10.1016/j.jog.2009.09.029. new Challenges in Earth's Dynamics - Proceedings of the 16th International Symposium on Earth Tides.

Tang, J., Cheng, H., Liu, L., 2014. Assessing the recent droughts in southwestern China using satellite gravimetry. Water Resources Research 50, 3030–3038.

https://doi.org/10.5194/egusphere-2026-975
Preprint. Discussion started: 27 March 2026

Tangdamrongsub, N., Steele-Dunne, S.C., Gunter, B.C., Ditmar, P.G., Sutanudjaja, E.H., Sun, Y., Xia, T., Wang, Z., 2017. Improving estimates of water resources in a semi-arid region by assimilating GRACE data into the PCR-GLOBWB hydrological model. Hydrology and Earth System Sciences 21, 2053–2074.

Tapley, B.D., Bettadpur, S., Ries, J.C., Thompson, P.F., Watkins, M.M., 2004. GRACE measurements of mass variability in the earth system. science 305, 503–505.

Tapley, B.D., Watkins, M.M., Flechtner, F., Reigber, C., Bettadpur, S., Rodell, M., Sasgen, I., Famiglietti, J.S., Landerer, F.W., Chambers, D.P., et al., 2019. Contributions of GRACE to understanding climate change. Nature climate change 9, 358–369. doi:https://doi.org/10.1038/s41558-019-0456-2.

Thomson, D.J., 1982. Spectrum estimation and harmonic analysis. Proceedings of the IEEE 70, 1055–1096. doi:10.1109/PROC.1982.12433.

Van Der Knijff, J., Younis, J., De Roo, A., 2010. LISFLOOD: a GIS-based distributed model for river basin scale water balance and flood simulation. International Journal of Geographical Information Science 24, 189–212.

Velicogna, I., 2009. Increasing rates of ice mass loss from the greenland and antarctic ice sheets revealed by GRACE. Geophysical Research Letters 36.

Vishwakarma, B.D., Bates, P., Sneeuw, N., Westaway, R.M., Bamber, J.L., 2021. Re-assessing global water storage trends from GRACE time series. Environmental Research Letters 16, 034005. doi:https://doi.org/10.1088/1748-9326/abd4a9.

Wada, Y., van Beek, L.P., Bierkens, M.F., 2012. Nonsustainable groundwater sustaining irrigation: A global assessment. Water Resources Research 48. doi:10.1029/2011WR010562.

Walvoord, M.A., Voss, C.I., Wellman, T.P., 2012. Influence of permafrost distribution on groundwater flow in the context of climate-driven permafrost thaw: Example from Yukon Flats Basin, Alaska, United States. Water Resources Research 48, W07524. doi:10.1029/2011WR011595.

Wang, H., Jia, L., Steffen, H., Wu, P., Jiang, L., Hsu, H., Xiang, L., Wang, Z., Hu, B., 2013. Increased water storage in North America and Scandinavia from GRACE gravity data. Nature Geoscience 6, 38–42.

Wang, J., Song, C., Reager, J.T., Yao, F., Famiglietti, J.S., Sheng, Y., MacDonald, G.M., Brun, F., Schmied, H.M., Marston, R.A., et al., 2018. Recent global decline in endorheic basin water storages. Nature geoscience 11, 926–932.

Wang, S., Zhou, F., Fatolazadeh, F., Russell, H., Bunn, M., 2025. Accelerated water loss over Canada's landmass in 2002–2024 .

Wang, X., de Linage, C., Famiglietti, J., Zender, C.S., 2011. Gravity Recovery and Climate Experiment (GRACE) detection of water storage changes in the Three Gorges Reservoir of China and comparison with in situ measurements. Water Resources Research 47. doi:https://doi.org/10.1029/2011WR010534.

Werth, S., White, D., Bliss, D., 2017. GRACE detected rise of groundwater in the Sahelian Niger River basin. Journal of Geophysical Research: Solid Earth 122, 10–459.

https://doi.org/10.5194/egusphere-2026-975
Preprint. Discussion started: 27 March 2026

Wouters, B., Gardner, A.S., Moholdt, G., 2019. Global glacier mass loss during the GRACE satellite mission (2002-2016). Frontiers in earth science 7, 96.

Wright, S.N., Thompson, L.M., Olefeldt, D., Connon, R.F., Carpino, O.A., Beel, C.R., Quinton, W.L., 2022. Thaw-induced impacts on land and water in discontinuous permafrost: A review of the Taiga Plains and Taiga Shield, northwestern Canada. Earth-Science Reviews 232, 104104.

Xanke, J., Liesch, T., 2022. Quantification and possible causes of declining groundwater resources in the Euro-Mediterranean region from 2003 to 2020. Hydrogeology Journal 30, 379–400.

Yang, X., Tian, S., Feng, W., Ran, J., You, W., Jiang, Z., Gong, X., 2020. Spatio-temporal evaluation of water storage trends from hydrological models over australia using GRACE mascon solutions. Remote Sensing 12, 3578.

Yang, Y., Long, D., Guan, H., Scanlon, B.R., Simmons, C.T., Jiang, L., Xu, X., 2014. GRACE satellite observed hydrological controls on interannual and seasonal variability in surface greenness over mainland australia. Journal of Geophysical Research: Biogeosciences 119, 2245–2260.

Yao, C., Luo, Z., Wang, H., Li, Q., Zhou, H., 2016. GRACE-derived terrestrial water storage changes in the inter-basin region and its possible influencing factors: A case study of the Sichuan Basin, China. Remote Sensing 8, 444.

Zemp, M., Chao, Q., Han Dolman, A.J., Herold, M., Krug, T., Speich, S., Suda, K., Thorne, P., Yu, W., 2022. GCOS 2022 Implementation Plan. Global Climate Observing System GCOS , 85doi:https://doi.org/10.5167/uzh-224271.

Zemp, M., Huss, M., Thibert, E., Eckert, N., McNabb, R., Huber, J., Barandun, M., Machguth, H., Nussbaumer, S.U., Gärtner-Roer, I., et al., 2019. Global glacier mass changes and their contributions to sea-level rise from 1961 to 2016. Nature 568, 382–386.

Zemp, M., Welty, E., 2023. Temporal downscaling of glaciological mass balance using seasonal observations. Journal of Glaciology doi:10.1017/jog.2023.66.

Zhao, K., Li, X., 2017. Estimating terrestrial water storage changes in the tarim river basin using GRACE data. Geophysical Journal International 211, 1449–1460.

Zhao, Q., Zhang, B., Yao, Y., Wu, W., Meng, G., Chen, Q., 2019. Geodetic and hydrological measurements reveal the recent acceleration of groundwater depletion in North China Plain. Journal of Hydrology 575, 1065–1072. doi:10.1016/j.jhydrol.2019.06.016.

Zhong, Y., Bai, H., Feng, W., Lu, J., Humphrey, V., 2023. Separating the precipitation- and non-precipitation-driven water storage trends in china. Water Resources Research 59, e2022WR033261.